ORIGINAL ARTICLE

Continued P2X7 activation leads to mitochondrial fission and compromising microglial phagocytosis after subarachnoid haemorrhage

Tao Tao[1] | Xiangxin Chen[2] | Yan Zhou[2] | Qiang Zheng[1] | Sen Gao[2] | Jinwei Wang[3] | Pengfei Ding[1] | Xiaojian Li[2] | Zheng Peng[2] | Yue Lu[2] | Yongyue Gao[2] | Zong Zhuang[2] | Chun-hua Hang[1,2] [ID] | Wei Li[1,2] [ID]

[1]Department of Neurosurgery, Nanjing Drum Tower Hospital Clinical College of Nanjing Medical University, Nanjing, Jiangsu Province, China

[2]Department of Neurosurgery, Nanjing Drum Tower Hospital, The Affiliated Hospital of Nanjing University Medical School, Nanjing, Jiangsu Province, China

[3]Department of Neurosurgery, Nanjing Drum Tower Hospital Clinical College of Jiangsu University, Nanjing, Jiangsu Province, China

Correspondence
Wei Li and Chun-hua Hang, Department of Neurosurgery, Nanjing Drum Tower Hospital, No. 321 Zhongshan Road, 210008, Nanjing, Jiangsu Province, China.
Email: wei.li@nju.edu.cn; hang_neurosurgery@163.com

Abstract

Subarachnoid haemorrhage (SAH) has a high rate of disability and mortality. Extremely damaging molecules, including adenosine triphosphate (ATP), are released from extravasated red blood cells and nerve cells, which activate microglia and induce sterile tissue injury and organ dysfunction. P2X purinoceptor 7 (P2X7) is one of the most important purine receptors on the microglial surface and is involved in the proinflammatory activation of microglia. While P2X7 can also affect microglial phagocytosis, the mechanism is not clear. Here, we demonstrated that microglial phagocytosis is progressively impaired under continued BzATP exposure and P2X7 activation. Furthermore, we found that P2X7 activation leads to increased intracellular Ca^{2+} levels and activates Calcineurin, which dephosphorylates dynamin-related protein 1 (DRP1) S637. The dephosphorylation of DRP1 at S637 leads to increased mitochondrial fission and decreased mitochondrial function, which may be responsible for the decreased microglial phagocytosis. Finally, we pharmacologically inhibited P2X7 activation in mice, which resulted in rescue of mitochondrial function and decreased microglial proliferation, but improved phagocytosis after SAH. Our study confirmed that P2X7 activation after SAH leads to the impairment of microglial phagocytosis through mitochondrial fission and verified that P2X7 inhibition restores microglial phagocytosis both in vitro and in vivo.

KEYWORDS
microglia, mitochondrial dynamics, P2X7, phagocytosis, subarachnoid haemorrhage

1 | INTRODUCTION

The annual number of strokes and deaths because stroke increased substantially among people older than 70 years. Subarachnoid haemorrhage (SAH) accounts for only 9.7% of all strokes, but it has a high rate of disability and fatality (Etminan et al., 2019). Most SAH patients are left with cognitive impairment and even disability, which seriously impairs their quality of life (Macdonald & Schweizer, 2016). The accumulation of damaging molecules after SAH aggregates the injury and limits repair (Garland et al., 2016). In the acute phase after SAH, damaging molecules that are released by blood components and injured nerve cells continuously trigger neuroinflammation (Schallner et al., 2015, p. 1), while in the repair phase, the presence of some damaging molecules, such as myelin inhibitory protein, inhibit nerve repair and compromise the neurological prognosis of SAH (Ballabh & de Vries, 2021; Pang et al., 2019). Improving the clearance of damage-inducing molecules is a promising direction in the treatment of SAH (Lan et al., 2017).

Microglia are the main phagocytes within the central nervous system (CNS), and their phagocytosis is the key for maintaining brain homeostasis (Colonna & Butovsky, 2017; Priller & Prinz, 2019; Wolf et al., 2017). Studies have shown that decreased microglial phagocytosis is closely related to the development of a variety of neurological diseases (d'Errico et al., 2021; Lloyd et al., 2019; Podleśny-Drabiniok et al., 2020). Decreased clearance of damaged molecules after TBI is one of the causes of impaired myelin repair (Van Broeckhoven et al., 2021). In multiple sclerosis, impaired myelin clearance because of insufficient microglial phagocytosis is an important factor in the recurrent development of the disease (Sen et al., 2022). In SAH, microglial phagocytosis appears to be restricted but remains controversial (Chen et al., 2022; Rudolph et al., 2021; Schallner et al., 2015, p. 1). Therefore, studies to clarify the role of microglial phagocytosis in SAH and explore the mechanisms involved are urgently needed.

Adenosine triphosphate (ATP) is a typical damaging molecule that is released from erythrocytes and injured neurons immediately after SAH, and there is an increased concentration of ATP at the injury site (Rodrigues et al., 2015). This ATP recruits distal microglia and initiates subsequent neuroinflammation (Davalos et al., 2005). P2X purinoceptor 7 (P2X7) is the most important purine receptor in microglia and can trigger Ca^{2+} influx after stimulation with ATP to initiate subsequent cellular physiological processes (McCarthy et al., 2019). P2X7 is involved in several physiological processes, such as the survival and differentiation of T lymphocytes (Borges da Silva et al., 2020; Romagnani et al., 2020), the activation of the NLR family pyrin domain containing 3 (NLRP3) inflammasome in macrophages/microglia (Martínez-García et al., 2019), and the release of inflammatory cytokines and chemokines (Shieh et al., 2014). Interestingly, it has been found that P2X7 activation is associated with impaired microglial phagocytosis of fibrillar Aβ, but the specific mechanism has not been elaborated (Francistiová et al., 2020). Here, we aimed to clarify the effect of P2X7 activation on microglial phagocytosis under continuous stimulation with ATP after SAH and to clarify the mechanism.

2 | METHODS AND MATERIALS

This study was approved by the local ethics committee (No. 2021-282-02 and No. 2020-041-01), and all enrolled subjects signed written informed consent forms. Inclusion and Exclusion Criteria in these two trials are listed in Tables S1 and S2. The patients' specimens were obtained from patients who had undergone internal decompression for a cerebral hernia after SAH, which was ethically reviewed by the unit where they were located. All animal procedures, including the use of avertin for mouse anaesthesia, were approved by the Ethics Review Committee for Animal Experimentation at Nanjing Drum Tower Hospital (No. 2020AE01064) and were conducted in accordance with recommendations from the *National Institutes of Health's Guide for the Care and Use of Laboratory Animals*.

2.1 | Enzyme-linked immunosorbent assay (ELISA)

For the detection of P2X7 in the patient's CSF, we chose Cusabio's Human P2X purinoceptor 7 ELISA kit (CSB-EL017325HU), which has a detection range of 25 pg/ml-1600 pg/ml.

Our pre-test results show that no additional dilutions are required for detection. Prepare reagents, samples and standards as instructed. Add 100 μl standard or sample to each well and incubate 2 h at 37°C. Remove the liquid of each well with no wash. Add 100 μl Biotin-antibody to each well and incubate 1 h at 37°C. Aspirate and wash 3 times. Add 100 μl HRP-avidin to each well and incubate 1 h at 37°C. Aspirate and wash 5 times. Add 90 μl TMB substrate to each well. Incubate 10–30 min at 37°C. Protect from light, avoid excessive incubation. Add 50 μl stop solution to each well and read at 450 nm within 5 min.

2.2 | Mice and SAH model

A total of 101 adult male C57BL/6 mice (RRID:IMSR_JAX:000664, 8–10 weeks old, 20–25 g), and ~100 pups within the first day of life from Animal Core Facility of Nanjing Medical University were used. No sample calculation was performed, the sample size determination was based on our own previous studies (Schüller et al., 2013; Tao et al., 2019). Post-hoc power analysis was performed in clinc alc.com for validating the sample size used (with α = 0.05 and an acceptable statistical power of 80%). This study was not pre-registered and no blinding was performed for the experimental design. Animals were allowed ad libitum access to food and water and kept in specific pathogen-free and comfortable conditions (12-h light/dark cycle, temperature at 25°C, and humidity at 65%) throughout the experiments. All animal experiments were conducted in daytime. Simple randomization was performed to assign animals to groups. N mice were assigned with Number from 1 to n (without repetition), and n random numbers were generated using *Rand()* in Excel. Random numbers were sorted and mice were assigned to each experimental group based on the sorted random numbers (e.g., the top 5 into the control group, next 10 into the SAH group).

The intravascular puncture model was operated by the same skilled experimenter (Tao et al., 2019). Animals were anaesthetized with 3% isoflurane (RWD # R510-22, Shenzhen) for its safety advantage, which was initiated through inhalation and maintained with 1.5% isoflurane during surgery. Meloxicam (5 mg/kg) were given subcutaneously after anaesthesia for pain relief. Mice were placed on a heating pad to maintain body temperature throughout the operation (body temperature was monitored by an anal temperature sensor). The external carotid artery (ECA) was ligated and divided slightly distal to the bifurcation, with an indwelled knot. The vessel was cut close to the broken end, and a prelabelled monofilament (CinoTech # 1620-5, Beijing) was inserted from the ECA in the reverse direction through the internal carotid artery to the middle cerebral artery bifurcation. In the SAH group, the monofilament was quickly inserted into a length of thread with a slight breakthrough sensation and was then withdrawn; the monofilament was directly withdrawn in the sham operation. The knots were tied to prevent bleeding. 1 ml saline intraperitoneally immediately after the operation. After surgery, the mice were placed in the animal's postoperative care chamber until they fully awoke, and jelly were given to the mice to supplement energy and water. Neurological function was assessed using the modified Garcia (mGarcia) score 24 h after surgery, and mice scoring ≤6 or ≥15 were excluded.

JNJ-47965567 (JNJ for short, MedChemExpress # HY-101418, Shanghai) was chosen to inhibit P2X7 because of its high efficiency, high specificity and ability to penetrate the blood brain barrier (Jimenez-Pacheco et al., 2016). JNJ was administered intraperitoneally at 30 mg/kg, bid, for 3 consecutive days. In SAH mice, continuous injection was performed for 3 days after modelling.

2.3 | Experimental design

The animal experimental design was divided into two parts (Figure S1). The first part evaluated the changes in P2X7 expression after SAH, (a) mice were first randomly divided into four groups ($n = 5$ in sham, $n = 8$–9 in SAH), then SAH model was performed and incompetent animals were excluded according to the mGarcia score, and finally 5 mice were included in each group, respectively. Brain tissues were taken for subsequent analysis after sacrifice with an overdose of isoflurane at 1 day, 3 days, and 7 days after SAH. (b) WB preliminarily determined significant changes at 3 days after SAH, so we chose 3 days after SAH in IF ($n = 5$ in sham, $n = 6$ in SAH 3d), and finally 5 and 3 mice, respectively, were included in the subsequent study.

The second part evaluated the effects of JNJ on microglial activation and phagocytosis in mice. (c) Mice were randomly assigned into two groups: one group received continuous intraperitoneal injection of vehicle ($n = 3$) and one group received continuous intraperitoneal injection of JNJ ($n = 5$); (d) in phagocytosis assessment, 3 days after SAH were selected for observation, one group received continuous administration of JNJ for 3 days after SAH ($n = 10$), and the other group received continuous administration of vehicle ($n = 10$), 6 mice

were included in the subsequent analysis, respectively; (e) in the last experiment, on the basis of the above design, stereotactic injection of DiO 24 h after SAH ($n = 6$–7) was performed, and 4 mice were included in the subsequent analysis, respectively. (f) 9 mice treated with JNJ (4 included) after SAH, 8 mice after SAH (4 included) and 4 sham mice (4 included) were included in the EM.

2.4 | Primary microglial culture and in vitro model

Culture medium preparation was performed as follows: high glucose Dulbecco's Modified Eagle Medium (DMEM, Gibco # C11995500BT) with 10% fetal bovine serum (FBS, Gibco #10099141C) and 1% penicillin–streptomycin (Gibco # 10378016). Within the first day of life, the pups were disinfected and decapitated, and the meninges were carefully removed and placed on ice. All the brains were pooled together and carefully cut into approximately 1 mm^3 pieces before TrypLE (Gibco # 12563029, Suzhou) was added for digestion at 37°C for 10 min. Digestion was stopped by adding 2 ml of FBS. The tissue was pipetted 10 times and filtered through a 70 μm strainer (Falcon #352350) and repeated 3–4 times. The filtrated cells were centrifuged at 1000 rpm for 5 min. After centrifugation, the supernatant was discarded, the cells were resuspended in culture medium and transferred to culture flasks. Approximately, cells from one mouse were transferred to one culture flask. The solution was refreshed on days 3 and 7, the microglia matured on approximately day 10, and suspended microglia were collected and transferred to well plates for subsequent experiments.

ATP stimulation of microglia was used as an in vitro model in our experiment. Considering the poor stability of ATP, we adopted a more stable BzATP instead of ATP. More than one study found that 100 μM BzATP (Topscience # TP2226, Shanghai) can significantly activate P2X7 and change the cell membrane potential, so we also used the same concentration (Coddou et al., 2011). Both JNJ-47965567 (100 nM), Mdivi-1 (10 μM, MedChemExpress #HY-15886, Shanghai) and FK506 (1 μM, MedChemExpress #HY-13756, Shanghai) were added to the culture medium 24 h in advance.

2.5 | Western blotting

The SAH mouse model was sacrificed through an overdose of isoflurane inhalation after treatment, and 20 mg of brain tissue in the temporal lobe of the injured hemisphere was collected after transcardial perfusion and was homogenized with RIPA (Beyotime #P10013B) and protease inhibitors (epizyme #GRF102). For the microglia, the cells were thoroughly detached using a cell curette, the supernatant was collected, loading buffer was added, and the cells were heated to denature the proteins. For western blotting, equal amounts of protein were added to each well for electrophoresis, separated until the bands of interest were clear, and then transferred to PVDF membranes. Blocking was performed using 2% bovine albumin for 2 h at 25°C, and primary antibodies were added after three TBST washes and were incubated

overnight at 4°C. The next day, the antibody was removed and washed three times with TBST, and the secondary antibody corresponding to the primary antibody was added and incubated for 2 h at 25°C. Antibodies used in WB: anti-P2X7 (Abcam, ab259942), anti-DRP1 (Cell Signaling Technology Cat# 8570, RRID:AB_10950498), anti-DRP1 S616 (Cell Signaling Technology Cat# 3455, RRID:AB_2085352), anti-DRP1 S637 (Cell Signaling Technology Cat# 6319, RRID:AB_10971640), anti-β tublin (Abmart Cat# M30109, RRID:AB_2916070), anti-β actin (Bioworld Technology Cat# AP0060, RRID:AB_2797445), anti-Calcineurin (ABclonal Cat# A1063, RRID:AB_2758155). Band analysis with the Fiji 2.0 (RRID:SCR_002285) Gel tool. The background subtraction was performed first, and the Rolling ball radius was set to 50 pixels, then the measurements were obtained.

2.6 | Immunofluorescence (IF), image acquisition, and analysis

The brain tissues of the patients were preserved in paraformaldehyde (PFA, Servicebio # G1101) and cut into 4 μm sections. The sections were deparaffinized by a xylene gradient before staining and were immersed in 10 mM sodium citrate for microwave heating to retrieve antigens. The mouse SAH model was sacrificed through inhalation of excessive isoflurane after the corresponding treatment, and the intact brain tissue was removed and placed in PFA for 24 h after transcardial perfusion was performed and was dehydrated using a sucrose gradient (15%, 30%). The frozen sections in thickness of 20 μm were blocked with 1% bovine albumin serum for 1 h at 25°C, followed by the addition of targeted primary antibodies and an incubation overnight at 4°C. After washing with PBS 3 times, fluorescent secondary antibodies corresponding to the source of primary antibodies were added, incubated for 2 h at 25° with protection from light, washed with PBS three times, and finally added to a fluorescence quencher containing DAPI and coverslipping. Antibodies used in IF: anti-Iba-1 (Abcam Cat# ab5076, RRID:AB_2224402), anti-P2X7 (Abcam Cat# ab259942, RRID: AB_2917969).

Fluorescence images were obtained with a Leica Thunder fluorescence microscope system and an Olympus FV3000 confocal microscope system. Images were analysed with Olympus CellSens software and ImageJ software. Imagej macros used in this manuscript is available online (https://github.com/NeurosurgeonTao/ImageJ_Macros).

In the phagocytosis assay, the cells were stained with Hoechst 33342 (Beyotime #C1027, Shanghai) for 10 min after the treatment, followed by fixation with PFA for 10 min, and images taken with a fluorescence microscope.

2.7 | CCK8 assay for cell viability

About 10% CCK8 (v/v, Vazyme #A311-02) diluted in the DMEM was added in the cell and incubate for 30–60 min in a 37°C incubator. Absorbance values were measured at 450 nm.

2.8 | Analysis of microglial branch length in 2D fluorescence pictures

In view of the 2D fluorescence pictures obtained under a common fluorescence microscope, microglial morphology analysis was studied with the help of Fiji. First, the image background was reduced ('Gaussian blur' and 'Image Subtract'), and with the help of the Ridge Detection plugin, the approximate morphology of microglial branches was delineated, followed by length measurement. Details are provided in the Supplementary Methods. Note that this analysis method is limited by the limitation of images and only provides limited reference value.

2.9 | Flow cytometry and calculation of phagocytic index

Before the phagocytosis experiment, the cells' original medium is discarded and washed 3 times with pre-warmed DMEM. the material to be phagocytosed for the assay is then added to the DMEM without FBS, mixed and added to each well, and incubated in a 37°C incubator for the subsequent assay (Gu et al., 2010).

Microglial phagocytosis was observed using flow cytometry. After the microglial cells were treated with phagocytic substances for 45 min, they were washed three times with DMEM, followed by digestion with 0.25% trypsin at 37°C for 10 min. The digestion was terminated with an appropriate amount of DMEM that contained 10% FBS and with gentle blowing to detach all cells. The cells were collected and centrifuged at 1000 rpm at 4°C for 8 min. After discarding the supernatant, 100 μl of DMEM that contained 1% FBS was added for resuspension and the supernatant was placed at 4°C in the dark for detection. Flow cytometry was performed in a BD C6 Plus, and data analysis was performed using FlowJo 10.7 software (RRID:SCR_008520, BD company). Phagocytic index = proportion of positive cells × mean fluorescence intensity(Park et al., 2020), and the values were finally normalized to the control group for comparison between different experiments.

2.10 | 2D and 3D analysis of mitochondria

Mitochondrial staining was performed in living cells with MitoTracker Red (Thermo Fisher #M22425, Suzhou). MitoTracker Red working solution was diluted 1:10000, added to the cells, incubated at 37°C for 10 min protected from light, and washed 3 times with HBSS to remove excess MitoTracker Red. Excessive staining was avoided. Mitochondrial structures were subsequently scanned under an FV3000 confocal microscope.

Mitochondrial 2D features were analysed using Fiji software with the MiNA plugin (Valente et al., 2017). The branch length mean (the mean length of all the lines used to represent the mitochondrial structures) and summed branch lengths mean (the mean of the sum of the lengths of branches for each independent structure) were

collected for statistical analysis. Mitochondria was reconstructed based on Z-stack scan; the mitochondrial branch volume analysis was semi-automatic performed in Fiji (macros provided below).

2.11 | Intracellular calcium measurement

Ca^{2+} levels in microglia were observed in vitro with the aid of the calcium indicator Fluo-8 AM (AAT Bioquest # 21080, Sunnyvale). Fresh Fluo-8 AM working solution (5 μM) was added into the cell plate and incubated in the dye-loaded plate in a cell incubator at 37°C for 30 min. The dye working solution with HHBS was replaced. BzATP was added and simultaneouslyfluorescence was measured using a fluorescence plate reader at 490/525 nm cutoff 515 nm.

2.12 | ATP assay

ATP was determined with the ATP detection kit (Beyotime #S0026); the kit is based on the principle that luciferase requires ATP to catalyse the production of fluorescence from luciferin. Cells were lysed and centrifuged at maximum speed on a microfuge for 5 min. The fraction supernatant was collected and tested for ATP levels with a luminometer.

2.13 | Reactive oxygen species (ROS) and mitochondrial membrane potential assay

About 10 μmoL/L DCFH-DA (Beyotime #S0033S, Shanghai) diluted with serum-free DMEM was added into the microglia. Positive control wells were set up by the addition of ROSUP. Incubated in a 37°C cell incubator for 20 min and mixed upside down every 5 min. Cells were washed three times with serum-free DMEM. Cells were then digested and collected to detect ROS levels by flow cytometry (FITC channel).

Mitochondrial membrane potential was detected with tetramethylrhodamine, ethyl ester, perchlorate (TMRE, Thermofisher #T669, Suzhou)(Crowley et al., 2016). After the cells were treated accordingly, cells are harvested and resuspended at 5×10^5 cells/ml in a culture medium containing 200 nM TMRE. Incubated for 5 min at 25° in the dark: 5 μM FCCP was added to control cell samples and incubated for 10 min as a positive control. Analysed with a flow cytometer using 488 nm laser for excitation and at emission 575 nm.

2.14 | Calcineurin activity assay

Calcineurin (CaN) activity was detected by colorimetric assay (Jiancheng Bio #A068-1-1, Nanjing). The test was performed according to the protocol. The supernatant was added to the chromogenic reagent to determine the absorbance at 636 nm. The activity unit of one CaN was specified as the amount of 1 μmol of inorganic phosphorus produced per hour per mg of protein by the CaN-decomposing substrate p-nitrophenyl phosphate (PNPP). CaN viability was determined by optical density (OD). CaN viability = (OD of test tube – OD of control tube)/ (OD of labelling tube – OD of blank tube)×concentration of standard substance (0.1 μmol/ml)×5×3/protein concentration of sample to be tested (mg prot/ml).

2.15 | Drp1 RNA interference and Drp1-phosphomicking mutant

We constructed lentiviral vectors expressing Drp1-specific shRNA to knock down DRP1 in BV-2 cells (pSLenti-U6-shRNA (Dnm1l)-CMV-F2A-Puro-WPRE, pSLenti-U6-shRNA (NC2)-CMV-F2A-Puro-WPRE, Obio-tech).

Serine at DRP1 locus 637 (locus 637 in human, locus 617 in mouse, mouse NM_152816.3 transcript) was mutated to aspartic acid (S637D) and constructed a lentiviral overexpression vector as a Drp1-phosphomicking mutant (pcSLenti-EF1-P2A-Puro-CMV-MCS-3xFLAG-WPRE, pcSLenti-EF1-P2A-Puro-CMV-Dnm1l [S617D]-3xFLAG-WPRE, Obio-tech).

BV-2 was obtained from from Shanghai Zhong Qiao Xin Zhou Biotechnology Co. (RRID: CVCL_0182, not reported in the International Cell Line Authentication Committee). No further authentication was performed in the laboratory. BV-2 less than 5 passages were seeded in 24-well plate at a density of 10^5 cells per well and transfected after 12 h of growth. In our experience, the MOI for BV-2 transfection was selected as 20 and polybrene (5 μg/ml) was added to increase transfection efficiency, the medium was changed after 24 h transfection. Screening was carried out by puromycin (5 μg/ml) starting 72 h after transfection for 1 week. The extent of shRNA-mediated knock-down of DRP1 expression was evaluated by western blotting analysis.

2.16 | Terminal deoxynucleotidyl transferase dUTP nick end labelling (TUNEL)

TUNEL staining was performed as previously published (Tao et al., 2019). The ratio of TUNEL+ cell in microglia: total TUNEL+ cell was evaluated in ImageJ.

2.17 | Acquisition of DiO-labelled cell debris

Neuronal cell debris were prepared for phagocytosis experiments using DiO/DiI-labelled HT-22 (RRID:CVCL_0321, from Shanghai Zhong Qiao Xin Zhou Biotechnology Co., not reported in the International Cell Line Authentication Committee) cell membranes(Wang et al., 2017). No further authentication was performed in the laboratory. HT-22 less than 5 passages were digested, counted, and centrifuged after the cells grew to full confluence. The cells were resuspended in HBSS with 1% nuclease (Beyotime #D7121, Shanghai), flash frozen directly in liquid

nitrogen, and immediately transferred to a 37°C water bath for rapid dissolution, which was repeated 3 times. The samples were centrifuged at 800 rpm for 5 min, and the supernatant was transferred and centrifuged again at 1, 500 rpm for 5 min to collect the precipitate. A DiO/DiI working solution was prepared according to the instructions, and then the solution was placed in a 37°C incubator for 15 min. Centrifugation was performed again at 1500 rpm for 5 min, the pellet was retained, 200 μl of DMEM was resuspended, and the solution was placed at –20°C until use with protection from light.

Stereotactic injection of resuspended DiO-labelled cell debris was performed by the same skilled experimenter (by Yan Zhou). In stereotactic experiments, the fixation of the mouse's teeth precludes use of an isoflurane inhalation mask. Therefore, avertin (375 mg/kg) was injected intraperitoneally for anaesthesia. To prepare the avertin solution, dissolve 2.5 g tribromoethanol in 5 ml amylene hydrate and heat dissolved solution to 40°C while stirring vigorously to get 12.5 mg/ml stock solution. Then dilute the stock solution with PBS to get a working solution at 20 mg/ml. Stock solution stored at –20°C in the dark for up to 1 year and working solution stored at 4°C in the dark for up to 2 weeks (McSweeney & Mao, 2015). We fixed the mouse on the stereotactic injector and exposed the skull. The right side of the anterior fontanel was located 1 mm, and the posterior side was 0.3 mm. After drilling with a milling cutter, a 10 μl Hamilton microsyringe needle was inserted 1.0 mm deep into the skull. A 3 μl volume injection was completed in 10 min, and the needle remained in place for 5 min after the injection.

2.18 | Electron micrograph

Brain specimens smaller than 1 mm^3 were stored in 2.5% glutaraldehyde. Afterward, they were postfixed flat in 1% osmium tetroxide and dehydrated in ascending concentrations of ethanol. They were treated with propylene oxide and then impregnated in resin overnight at 25°. After mounting, they were cured at 55°C for 72 h. Areas of interest were re-embedded at the tip of resin blocks and cut at 70 nm of thickness using an ultramicrotome. Ultrathin sections were collected and examined under a Hitachi transmission electron microscope at 80 kV (Savage et al., 2018).

2.19 | Statistics

All data were tested for normality with the Kolmogorov–Smirnov test and no test for outliers was conducted. Data that passed the normality test are expressed as the mean ± SEM. Data that were not normally distributed were expressed as the median (the 25th to the 75th percentile). Differences were considered statistically significant at $p < 0.05$. All analyses were performed in GraphPad Prism 8.0 (RRID:SCR_002798). Statistics information is available in Table S3.

3 | RESULTS

3.1 | Robust microglial activation accompanied by increased P2X7 expression after SAH

After SAH, many injured nerve cells and blood cells continuously release intracellular ATP, and P2X7 is the most important purine receptor in microglia. We first evaluated the expression of P2X7 in SAH patients. Limited by the availability of normal human brain tissue, distal sites in the same specimen were set as controls. After labelling microglia with Iba-1, we found that the microglia in SAH lesions were robustly activated, as indicated by a significant increase in density (Figure 1a, ~1-fold increase), rounding of the cell bodies, near disappearance of branching, and a twofold increase in diameter (Figure 1b, 7.189 (6.040, 8.180) μm vs. 7.005 (10.80, 16.91) μm, $p < 0.001$), all of which indicated that the microglia was substantially recruited and activated in the injured area after SAH. Moreover, distinct co-localization of P2X7 with Iba-1 was observed in these activated microglia, which disappeared in non-activated microglia at distant sites, suggesting that increased P2X7 expression occurred in the activated microglia after SAH. Similar results were observed in the SAH mouse brain sections (Figure 1d).

Subsequently, western blotting showed that P2X7 was significantly increased 1 day after SAH (Figure 1c, $p = 0.0077$), while the expression level peaked at 3 days after SAH ($p = 0.0043$) and remained high at 7 days. These results illustrate that microglial P2X7 expression is elevated in injured brain tissue after SAH, suggesting that microglial activation is possibly involved.

We also observed the changes of P2X7 in CSF of SAH patients (patients with non-brain tissue specimens), including 52 SAH patients and 6 controls, a total of 73 SAH CSF samples and 6 control samples (Table S4). Interestingly, we found no significant changes in CSF P2X7 after SAH (Figure 1e, 30.02 (5.082, 48.94) pg/ml vs. 7.005 (4.749, 12.11) pg/ml, $p = 0.150$), and we also did not observe a significant difference after distinguishing the patients with Hunt & Hess scores or mRS scores after 3 months of discharge (Figure S2). Combined with the aforementioned results, these changes in P2X7 may be limited to the microglia at the site of injury, and the P2X7 content in CSF remained unchanged.

Is increased microglial P2X7 expression accompanied by changes in related functions? The involvement of P2X7 in microglial synthesis and release of IL-1β was determined with certainty, so we also evaluated the IL-1β content in the CSF of patients after SAH and found that IL-1β was significantly increased (Figure 1f, 351.5 (323.4, 566.6) pg/ml vs. 4343 (2544, 10 505) pg/ml, $p < 0.001$). Although IL-1β does not specifically indicate changes in P2X7 function, it still supports P2X7 activation in SAH microglia.

3.2 | Continued P2X7 activation leads to decreased microglial phagocytosis

Many studies have shown that P2X7 activation promotes the microglial inflammatory response, but the effect of P2X7 on microglial
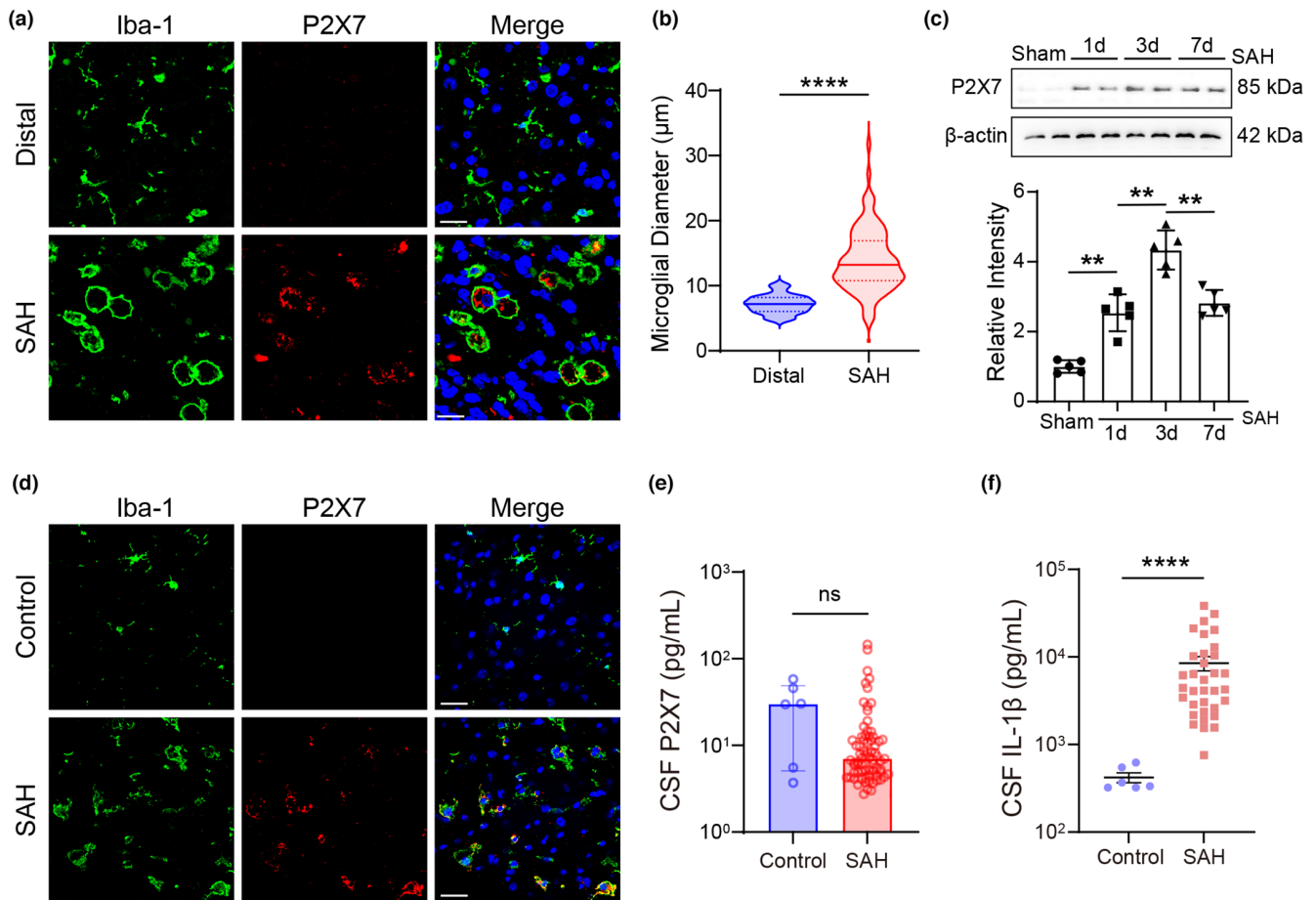
FIGURE 1 The expression of microglial P2X7 was elevated both in human and mice after SAH. (a) Sections of brain tissue from SAH patients at the sites of injury and distant sites were stained with Iba-1 (green) and P2X7 (red). (b) the diameter (in μm) of microglia was analysed. *N* denotes the number of microglia, *n* = 26 from distal and *n* = 97 from injury sites. Two-sided Mann–Whitney *U* test. (c) P2X7 expression in mouse SAH models (1 dpi, 3 dpi and 7 dpi) was assessed by western blotting. *N* denotes the number of animals, *n* = 5–6 mice per group. Brown-Forsythe ANOVA with Dunnett's T3 test. (d) Sections of brain tissue from mouse SAH models (3 dpi) were stained with Iba-1 (green) and P2X7 (red), respectively. (e) P2X7 and (f) IL-1β content in the CSF, *n* denotes the CSF samples from the SAH patients and the control. Two-sided Mann–Whitney U test. Dpi, days post injury. Scale bar = 30 μm in (a) and (d). Exact *p* values noted; ns, not significant, **$p < 0.01$; ***$p < 0.001$; ****$p < 0.0001$

phagocytosis was unclear. We directly assessed microglial phagocytosis in primary microglia under BzATP exposure. pHrodo *E. coli* particles and 10% CCK-8 (v/v) were added simultaneously at different times (2, 6, 12, 24, 36, and 48h) after BzATP exposure, and the relative fluorescence values (RFU) and absorbance were rapidly obtained under a fluorescence microplate reader after 45min of incubation. The readings suggested that microglial phagocytosis was transiently increased at 2 h of BzATP stimulation, then a gradual decrease was observed. The phagocytosis was lower than that of the control group after 36h of ATP stimulation (Figure 2a,b, 1457 ± 133.9 vs. 307.4 ± 128.3, *p* = 0.027) and did not decrease further. Furthermore, the CCK8 readings suggested a slight increase in cellular activity, but no significant difference from baseline, ruling out the possibility of a decrease in cellular viability following BzATP stimulation.

In contrast to the results of the microplate reader, the experiments in the flow cytometry for phagocytosis found that 2 h of BzATP stimulation caused a decrease in phagocytosis, although there was no significant difference (Figure S3a shows the gating

strategy; Figure 2c,d). Experiments using both pHrodo *E. coli* particles and DiO-labelled cell debris confirmed that a significant decrease in phagocytosis occurred at 6 h of ATP stimulation and an even more significant decrease at 24h of stimulation (*p* = 0.0016 in Figure 2c, *p* < 0.0001 in Figure 2d). We have observed a decrease in phagocytosis not only in primary microglia, but also in BV-2 cells (Figure S3b,c). We basically clarified the decreasing trend of microglial phagocytosis after BzATP stimulation.

To verify whether microglial phagocytosis changes upon BzATP stimulation in correlation with P2X7, we selected JNJ-47965567 (JNJ for short in the following)(Bhattacharya et al., 2013, p. 47965567), a specific inhibitor of P2X7, to block P2X7 and subsequently analysed phagocytosis 24h upon BzATP stimulation by flow cytometry. Both the pHrodo *E. coli* particles and DiO-labelled cell debris phagocytic assays suggested that JNJ was able to significantly reverse the decrease in phagocytosis, suggesting that P2X7 activation at least partially mediates the decrease in microglial phagocytosis (Figure 2e–f, *p* < 0.0001 and *p* = 0.0138).
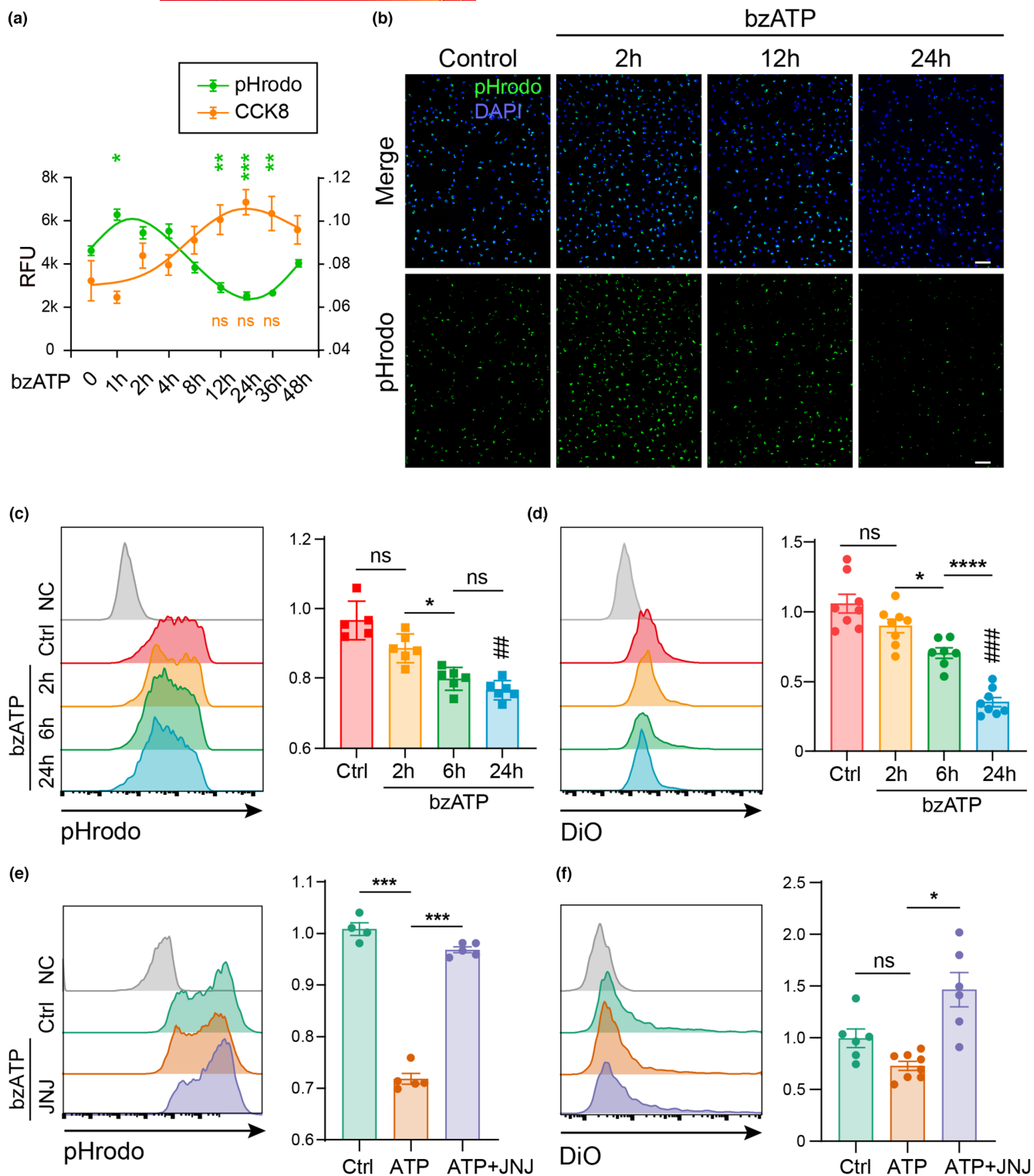
3.3 | Mitochondrial fission after P2X7 activation leads to decreased microglial phagocytosis

Although studies have reported that P2X7 may be involved in the phagocytosis of macrophages/microglia(Gu & Wiley, 2018), it is not clear how P2X7, as a membrane receptor and calcium channel, affects microglial phagocytosis.

Here, we noticed that the morphology and function of microglial mitochondria are altered upon P2X7 activation and may be a potential mechanism that affects phagocytosis. After labelling mitochondria with MitoTracker Red (Figure 3a), MiNA analysis showed that the mitochondrial length was significantly shorter in P2X7-activated microglia both in the mitochondrial branch length mean (Figure 3b, 1.865 (1.637, 2.232) vs. (1.296 [1.168, 1.414] μm, $p < 0.001$)) and

FIGURE 2 Continued BzATP stimulation resulted in a gradual decrease in primary microglial phagocytosis. Microglia were continuously stimulated with BzATP for different periods (0, 1, 2, 6, 12, 24, 36, and 48 h), and pHrodo *E. coli* particles was incubated for 45 min. (a) the pHrodo intensity (green) and CCK8 (orange) absorbance was scanned with a fluorometer; (b) representative pictures under a fluorescence microscope (blue, DAPI). Scale bar = 100 μm. *N* denotes the number of independent cell culture preparations, n = 5–6 per group. Brown–Forsythe ANOVA and Dunnett's T3 test, # represents the comparison from ctrl. Microglia were stimulated with BzATP for different periods (0, 2, 6, 24 h), and then (c) the pHrodo *E. coli* particles or (d) DiO-labelled cell debris was added and incubated for 45 min. Then, the number and fluorescence intensity of positive cells were evaluated by flow cytometry, and the phagocytic index was calculated. *N* denotes the number of independent cell culture preparations, n = 5–6 per group. Microglia were pretreated with the P2X7-specific inhibitor JNJ-47965567 (JNJ for short in the panel) and were then stimulated with BzATP for 24 h, and (e) the pHrodo *E. coli* particles and (f) DiO-labelled cell debris were incubated for 45 min before the phagocytic index was observed with flow cytometry. *N* denotes the number of independent cell culture preparations, n = 4–6 per group. Brown–Forsythe ANOVA and Dunnett's T3 test, # represents the comparison between 24 h and Ctrl. NC, negative control; Exact *p* values noted; ns, not significant; ##*p* < 0.01; ###*p* < 0.001; **p < 0.05; **p < 0. 01; ***p < 0.001; ****p < 0.0001.

summed branch lengths mean (Figure 3c, 2.278 (1.866, 2.656) vs. (1.550 [1.415, 1.729] μm, *p* < 0.001)), suggesting that P2X7 activation influences mitochondrial fission and fusion. However, inhibition of P2X7 could effectively increase the mitochondrial length significantly (Figure 3b,c, 1.614 (1.382, 1.839) μm in branch length mean, *p* < 0.001; 1.918 (1.688, 2.175) μm in summed branch lengths mean, *p* < 0.001).

We also performed 3D reconstruction of mitochondria based on confocal Z-axis imaging (Figure S4). Our analysis found that the median of mitochondrial volume increased following ATP stimulation but was not significant (Figure 3d,e, 0.030 (0.014, 0.065) vs. 0.034 (0.013, 0.119) μm^3, *p* = 0.1193), whereas the increase in the mitochondrial branches number was significant (Figure 3d,e, 45.13 ± 6.831 vs. 90.33 ± 8.090, *p* = 0.0039). In contrast, JNJ treatment caused a decrease in branch number without significance. These results suggest that P2X7 activation may lead to excessive mitochondrial fission within microglia, which may be the main factor that affects microglial phagocytosis.

Mitochondrial dynamics (fission and fusion) are closely related to mitochondrial functions, and excessive mitochondrial fission can affect their membrane potential levels and limit their ATP production and cellular function. Thus, the question arose whether excessive mitochondrial fission is the main cause of decreased microglial phagocytosis after P2X7 activation. Mdivi-1 is a compound that acts on dynamin-related protein 1(DRP1) and effectively inhibits mitochondrial fission. We pretreated microglia with Mdivi-1, followed by BzATP and phagocytosis assays. First, it was clarified that Mdivi-1 reversed the excessive fission of mitochondria upon P2X7 activation (Figure 3a,c, 2.388 (2.089, 2.761) μm in branch length mean, *p* < 0.001; 2.872 (2.465, 3.319) μm in summed branch lengths mean, *p* < 0.001, both compared with ATP group). Then, we evaluated the effect of the reversal of mitochondrial hyperfission by Mdivi-1 on microglial phagocytosis and found that Mdivi-1 was able to ameliorate the decrease in phagocytosis that was induced by P2X7 (Figure 3f,g, *p* = 0.0002).

In addition to using inhibitor of DRP1, we also constructed DRP1 knockdown BV-2 cells and observed phagocytosis under decreased DRP1. The results showed a significant recovery of phagocytosis of DiI-labelled cell debris by BV-2 in the presence of DRP1 knockdown (Figure 3j,k, *p* = 0.0211). The above results illustrate that

mitochondrial fission may be a key event in P2X7 activation that leads to decreased microglial phagocytosis.

3.4 | Excessive mitochondrial fission leads to a decrease in membrane potential and ATP production

Mitochondrial fission and fusion are dynamic processes. Appropriate mitochondrial fission plays an important role in the mitotic process and mitochondrial turnover, but excessive fission may damage the function of mitochondria. To clarify the effect of P2X7-evoked mitochondrial fission on cells, we examined the mitochondrial membrane potential (MtMP) with TMRE staining. It was found that the MtMP decreased after BzATP stimulation (Figure 4a,b, 3.40 ± 0.17 × 10^6 vs. 2.24 ± 0.13 × 10^6, *p* = 0.0022), while inhibition of P2X7 alleviated the decrease (Figure 4a,b, 2.24 ± 0.13 × 10^6 vs. 3.90 ± 0.15 × 10^6, *p* < 0.001), and if mitochondrial fission was inhibited with the help of Mdivi-1, the change in MtMP was partially reversed (Figure 4a,b, 2.24 ± 0.13 × 10^6 vs. 3.11 ± 0.23 × 10^6, *p* = 0.019). Similar results were observed in BV-2 with DRP1 knockdown, although the decrease in TMRE following BzATP stimulation did not reach a significant difference (Figure 4c,d). JC-10 is another dye that shows MtMP, and the staining results of JC-10 are similar to those of TMRE (Figure 4e), confirming that the mitochondrial fission triggered after P2X7 activation impairs mitochondrial function.

An important marker of mitochondrial functional impairment is the production of reactive oxygen species (ROS), so we examined mitochondrial ROS production with DCFH-DA. The DCFH assay indicates a significant increase in ROS in both primary microglia (Figure 4g,h, 21 047 ± 335.6 vs. 36 186 ± 1605, *p* = 0.047) and BV-2 cells (Figure 4i,j, 1796 ± 113.6 vs. 7530 ± 596.8, *p* = 0.0157) following BzATP stimulation, and either specific inhibitors or knockdown were able to mitigate the elevated ROS.

Subsequently, we examined the direct form of intracellular energy, ATP. We found that the production of microglial intracellular ATP declined significantly after P2X7 stimulation, as we hypothesized (Figure 4f, 4.896 ± 0.392 vs. 3.048 ± 0.252 μmol/μg, *p* = 0.0177). However, intracellular ATP production increased after inhibition of both P2X7 activation (6.945 ± 0.413 μmol/μg, *p* = 0.002)
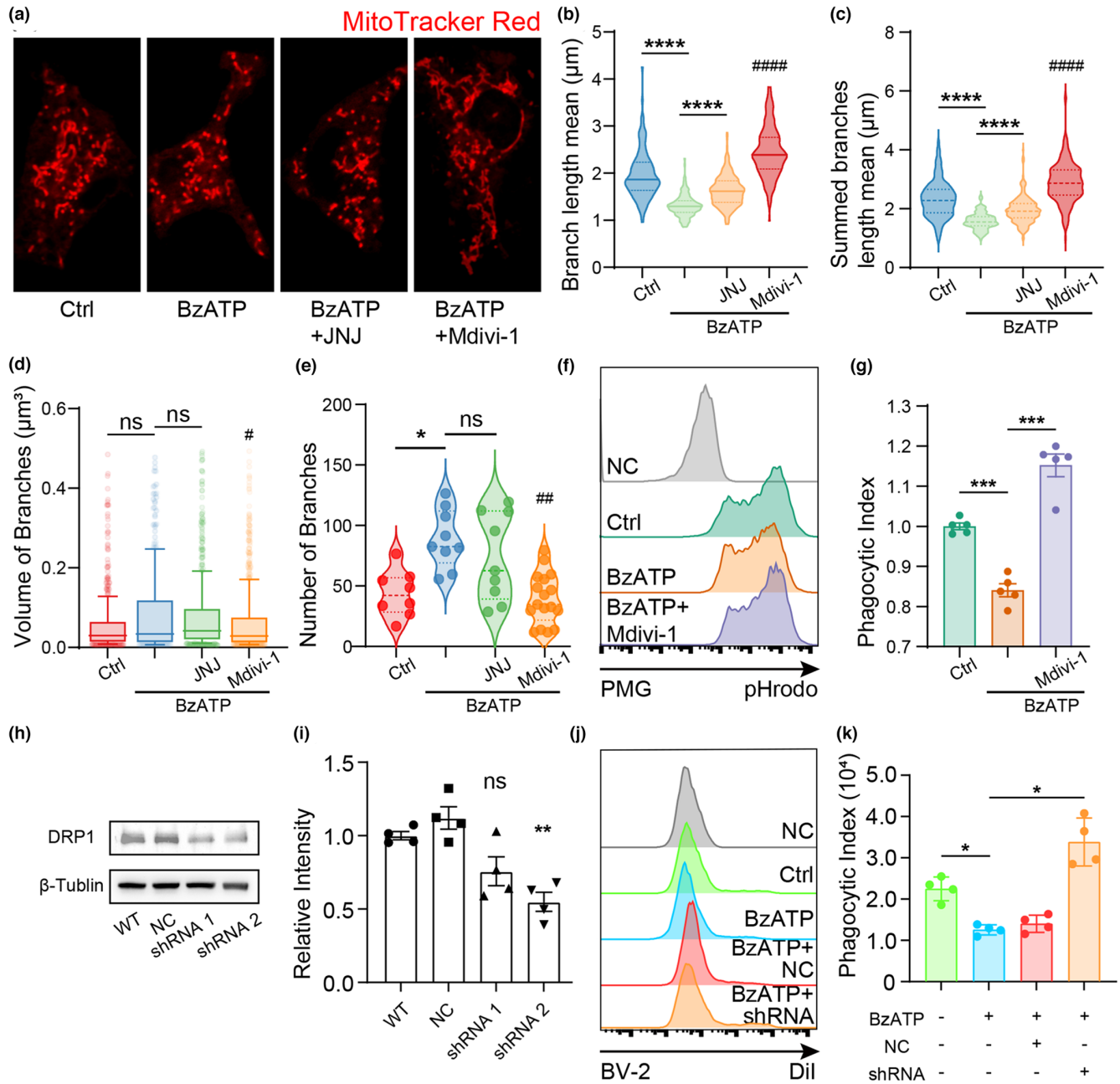
FIGURE 3 Excessive microglial mitochondrial fission after P2X7 activation may be associated with decreased phagocytosis. (a) Microglia were pretreated with JNJ-47965567 or Mdivi-1 followed by BzATP stimulation for 24 h and then labelled with MitoTracker red. (b) Branch length mean and (c) summed branches length mean were counted with MiNA plugin. N denotes the number of pictures, $n = 109–208$ of each group. (d) Display of all mitochondrial branch volumes in each group. Each dot indicates one mitochondrion. (e) The number of branches was analysed after 3D reconstruction. N denotes the number of microglia, $n = 8–17$ per group. (f, g & j, k) microglial phagocytosis after 24 h of BzATP stimulation was observed by flow cytometry. Microglia were pretreated with Mdivi-1 to prevent mitochondrial fission, and the phagocytic index was calculated. N denotes the number of independent cell culture preparations, $n = 4–6$ per group. (h, i) Western blotting for shRNA interference efficiency, comparisons between WT and shRNA. N denotes the number of pictures, $n = 4$ of each group. Kruskal–Wallis test with Dunn's test in panels (b–d) but Brown–Forsythe ANOVA and Dunnett's T3 test in panel (e–k). JNJ-47965567, JNJ for short in the panel; # represents the comparison between BzATP+Mdivi-1 and BzATP; exact p values noted; ns, not significant; #$p < 0.05$; ##$p < 0.01$; ####$p < 0.0001$; *$p < 0.05$; **$p < 0.01$; ***$p < 0.001$; ****$p < 0.0001$
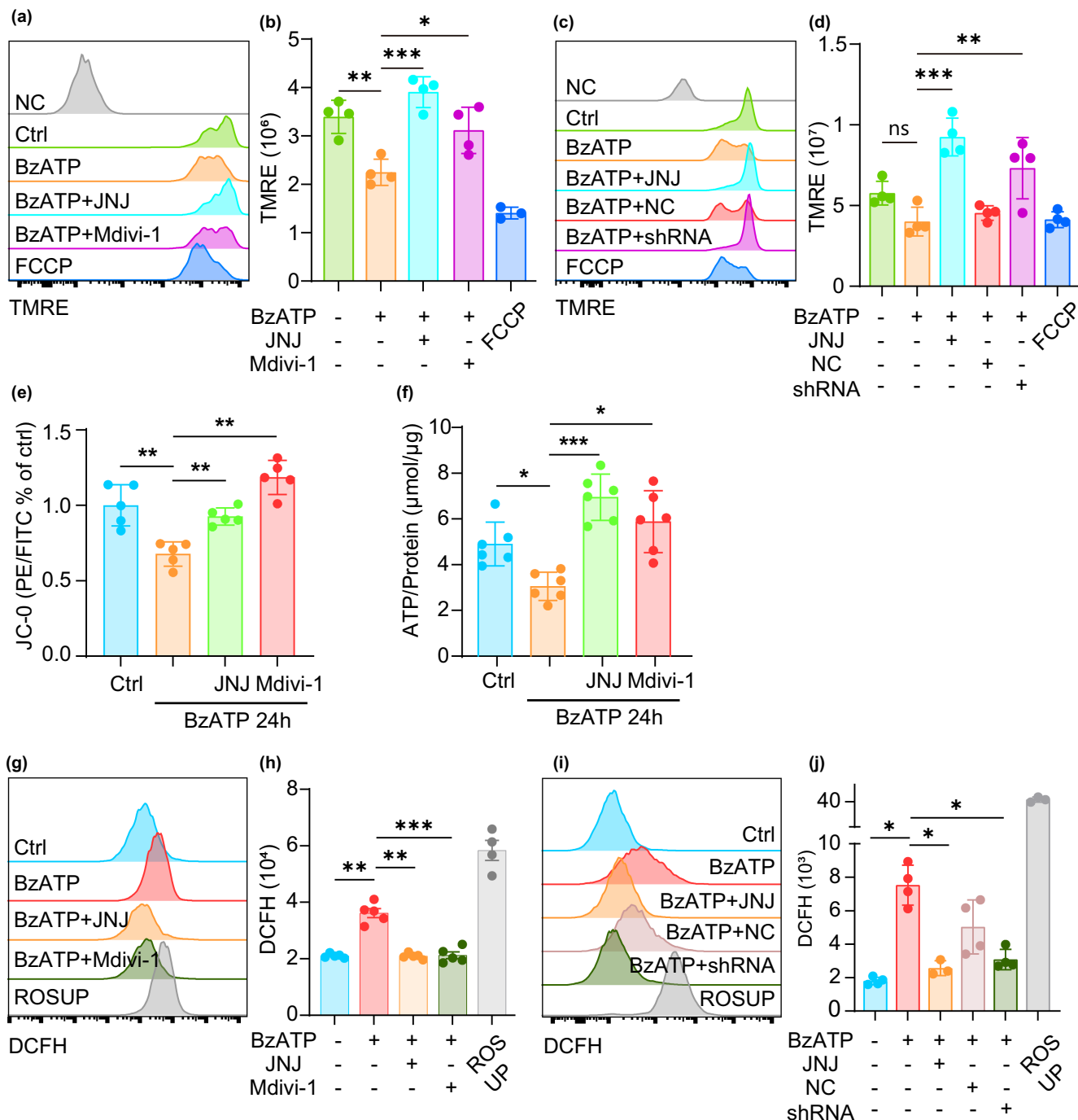
FIGURE 4 Excessive mitochondrial fission leads to decreased membrane potential (MtMP) and impaired ATP production. Microglia were treated with BzATP for 24 h with or without the presence of JNJ-47965567 or Mivi-1. Mitochondrial membrane potential was assessed with TMRE & JC-10 staining. (a, b) Primary microglial MtMP analysed by TMRE staining. FCCP was used as positive control. (c, d) BV-2 microglial MtMP analysed by TMRE staining. (e) The ratio of PE/FITC in JC-10 staining was calculated. (f) ATP production in microglia in the presence of P2X7-activated mitochondrial fission, and Mdivi-1 was used as a control. (g, h) Primary microglial ROS production analysed by DCFH. (j, k) BV-2 microglial ROS production analysed by DCFH. ROSUP was used as a positive control. N denotes the number of independent cell culture preparations, n = 4–6 per group. Brown–Forsythe ANOVA and Dunnett's T3 test. JNJ-47965567, JNJ for short in the panel; exact p values noted; *p < 0.05; **p < 0.01; ***p < 0.001

and mitochondrial fission (5.876 ± 0.553 μmol/μg, $p = 0.012$), even higher than the control group, but there was no difference between the JNJ and Mdivi-1 groups. These show that P2X7 activation promotes microglial mitochondrial fission, affects mitochondrial function, and reduces ATP production, finally compromising microglial phagocytosis.
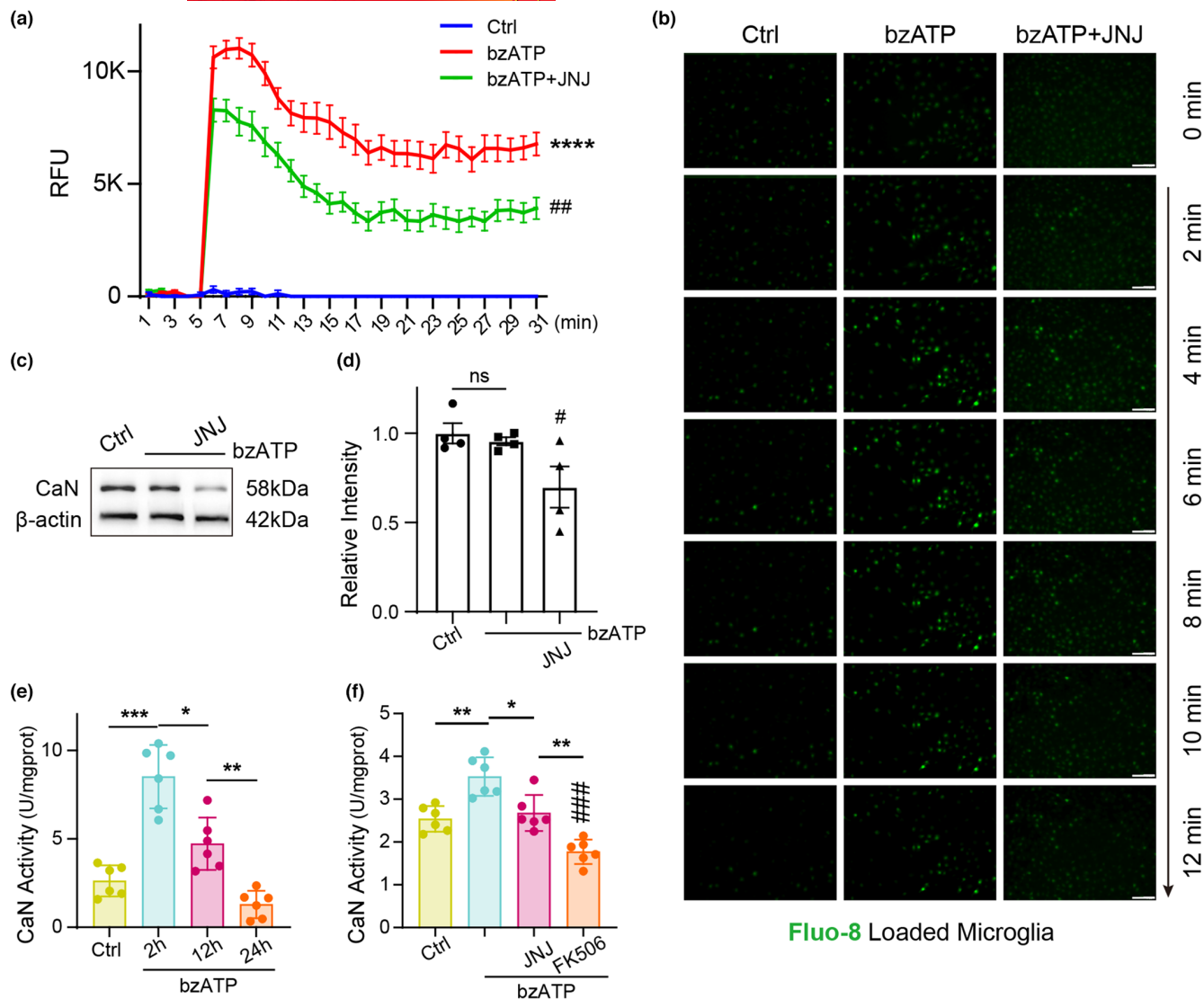
FIGURE 5 Activation of microglial P2X7 following BzATP stimulation triggers Ca^{2+} influx and activates CaN activity. The microglia were pre-loaded with Fluo-8 AM, a Ca^{2+} binding dye and stimulated with BzATP, the fluorescence intensity was real-time monitored by a fluorometer for 30 min. (a) Fluo-8 fluorescence intensity readings before and after BzATP stimulation. N denotes the number of independent cell culture preparations, $n = 4$ per group. Two-way ANOVA with Dunnett's test. (b) Representative Fluo-8 fluorescence pictures. Scale bar = 50 μm. (c, d) Western blotting was used to detect the changes in CaN protein expression in microglia stimulated with BzATP, and β-Actin was used as an internal reference. N denotes the number of independent cell culture preparations, $n = 4$ per group. One-way ANOVA with Tukey's test. (e) CaN activity was detected at different time points (0, 2, 6, and 24 h) after the primary microglia were stimulated with BzATP. N denotes the number of independent cell culture preparations, $n = 6$ per group. (f) CaN activity changes were observed under specific inhibition of P2X7 at 24 h BzATP exposure, and FK506 was used as a negative control. N denotes the number of independent cell culture preparations, $n = 6$ per group. Brown–Forsythe ANOVA with Dunnett's T3 test in panel (e, f). JNJ-47965567, JNJ for short in the panel; RFU, relative fluorescence units; exact p values noted; ns, not significant; $\#\#p < 0.001$; $\#\#\#p < 0.001$; $*p < 0.05$; $**p < 0.01$; $***p < 0.001$

3.5 | P2X7 mediates calcium influx and activates calcineurin

Although we found that P2X7 activation leads to mitochondrial dysfunction, the mechanism is unclear. To clarify the specific mode of P2X7 action under BzATP stimulation, it is first necessary to clarify the calcium channel function of P2X7, so we observed changes in intracellular calcium after BzATP stimulation. When BzATP was added to microglia which was pre-loaded with a calcium probe

(Fluo-8 AM), fluorescence dynamic observation revealed that the intracellular calcium content of microglia (RFU reading) was instantaneously and significantly increased (Figure 5a,b, 213.7 ± 74.19 vs. $10\,625 \pm 487.0$, $p < 0.0001$), followed by a gradual decrease; however, the level was still significantly higher than the baseline even after half an hour of observation (Figure 5a, 6 min, 213.7 ± 74.19 vs. 6779 ± 509.7, $p < 0.0001$). Furthermore, in microglia that were treated with JNJ to block P2X7, both the peak and plateau calcium elevation levels were significantly lower than those in the BzATP

group (Figure 5a, $10\,625\pm487.0$ vs. 8282 ± 513.0, $p<0.001$), indicating that blocking P2X7 with JNJ can inhibit calcium influx.

Increased intracellular calcium causes broad effects, and there is evidence that increased intracellular calcium affects mitochondrial fission by activating calcineurin (CaN)(Cereghetti et al., 2008). We assessed the protein expression and activity of CaN upon P2X7 activation. Western blotting analysis suggested that the levels of CaN protein did not change significantly after BzATP stimulation; however, the levels of CaN protein decreased significantly after JNJ and BzATP treatment (Figure 5c,d, $p=0.0472$). CaN activity assay revealed that the activity increased significantly 2 h after BzATP stimulation (Figure 5e, 2.629 ± 0.359 vs. $8.522\pm0.733\,U/mgprot$, $p=0.0009$), and CaN activity gradually decreased with stimulation time (Figure 5e, $p<0.05$). These results suggested that the activity of CaN was rapidly altered after BzATP stimulation, even before the change in phagocytosis.

Are changes in CaN activity associated with P2X7 activation? Subsequently, by specifically inhibiting P2X7, we assessed the changes in intracellular CaN activity in microglia after 2 h of BzATP stimulation and employed the CaN inhibitor FK506 as a negative control group. Upon testing, it was found that CaN elevation was significantly reversed after the JNJ treatment (Figure 5f, 3.526 ± 0.184 vs. $2.678\pm0.172\,U/mgprot$, $p=0.038$), while in the FK506 treatment group, CaN activity was significantly lower than that in the control group (Figure 5f, 1.771 ± 0.116 vs. $2.540\pm0.122\,U/mgprot$, $p=0.0057$). The above results all illustrate that P2X7 activation triggers an increase in intracellular CaN activity in microglia, which may be associated with subsequent mitochondrial fission.

3.6 | CaN regulates dephosphorylation at DRP1 S637 to promote mitochondrial fission

For mitochondrial fission to occur, some important dyneins must participate, and among the dyneins, dynamin-related protein 1(DRP1) plays the most important role. DRP1 acts through its GTPase activity, but its phosphorylation status has a decisive impact on its function, and the most predominant phosphorylation sites are S616 and S637. To determine whether P2X7 activation regulates mitochondrial fission through DRP1, we first evaluated the expression of DRP1 and its phosphorylation status after P2X7 activation (Figure 6a). Western blotting analysis revealed that DRP1 total protein and the phosphorylation level at position 616 were not significantly changed after P2X7 activation, but the protein was significantly dephosphorylated at position 637 (Figure 6b, $p=0.0006$), and this phosphorylation change disappeared in the presence of JNJ ($p=0.0182$), indicating that the change was triggered by P2X7 activation. Some studies have reported that CaN is involved in the dephosphorylation of DRP1 at S637 and promotes mitochondrial fission. Moreover, in the presence of FK506, the specific inhibitor of CaN, this treatment did prevent dephosphorylation at position 637 (Figure 6b, $p=0.0182$).

We also observed mitochondrial morphological changes after CaN activity was inhibited. Mitochondria length analysis demonstrated that FK506 alleviated mitochondrial hyperfission after P2X7 activation (Figure 6c,d, 1.409 (1.197, 1.744) vs. 1.718 (1.448, 2.023) μm in branch length mean, $p<0.0001$; 1.693 (1.397, 1.940) vs. 2.014 (1.689, 2.423) μm in summed branches length mean, $p<0.0001$). Flow cytometry further confirmed that microglial phagocytic dysfunction by BzATP was rescued by blocking the function of CaN (Figure 6e,f, 0.786 ± 0.030 vs. 1.014 ± 0.023, $p=0.0011$).

To further clarify the effect of the phosphorylation status of the DRP1 S637 on phagocytosis, we constructed the Drp1 S637 phosphomicking mutant (S637D) by overexpressing a transcript modified at site 637. Although western blotting showed successful overexpression of DRP1, the commercial anti-p637 antibody failed to recognize the change in p637 (Figure 6g). We suggest that this may be a failure of the antibody to recognise the mutated protein. Further phagocytosis assays revealed that S637D significantly improved microglia phagocytosis (Figure 6h,i, $37\,228\pm1783$ vs. $76\,549\pm4566$, $p=0.008$).

Here, we verified that increased CaN activity accelerates the dephosphorylation of DRP1 at S637, leading to mitochondrial hyperfission, which may be the molecular mechanism by which P2X7 activation leads to phagocytic dysfunction.

3.7 | Inhibition of P2X7 in vivo increases microglial phagocytosis after SAH

Experiments in primary microglia confirmed that inhibiting the continued activation of P2X7 can enhance microglial phagocytosis; therefore, is such an effect also present in mice? We inhibited P2X7 in C57BL/6 mice with JNJ. We first evaluated the effect of continuously injecting JNJ on microglia in WT mice. After IF labelling, we found that continuous administration of JNJ had no influences on the number (Figure 7a,b, $5.256\pm0.039\,\mu m$ vs. $5.357\pm0.037\,\mu m$, $p=0.0798$) or the morphology of microglia (Figure 7a,b, 38.51 ± 1.537 vs. 38.94 ± 1.036 microglia per field, $p=0.8177$) in the mice.

Subsequently, we observed microglial mitochondrial changes in in vivo with the aid of electron microscopy. In general, mitochondria are not very abundant in microglia, especially in the resting state, where the nucleus occupies most of the cell and the mitochondria are in a striped shape. After SAH, the microglial cell cytosol is significantly enlarged, mainly by a significant increase in the cytoplasmic contents. The mitochondria change to a granular shape, accompanied by an increase in number and partial structural disruption. In addition, vesicles that phagocytosed other material appeared in the cytoplasm, mostly suspected to be damaged myelin structures. In the JNJ-treated mice, the mitochondria were more clearly structured, larger, and held more phagocytic material within the cells.

Finally, we observed the effect of JNJ on the function of microglia after SAH in mice. We found that JNJ significantly inhibited microglial
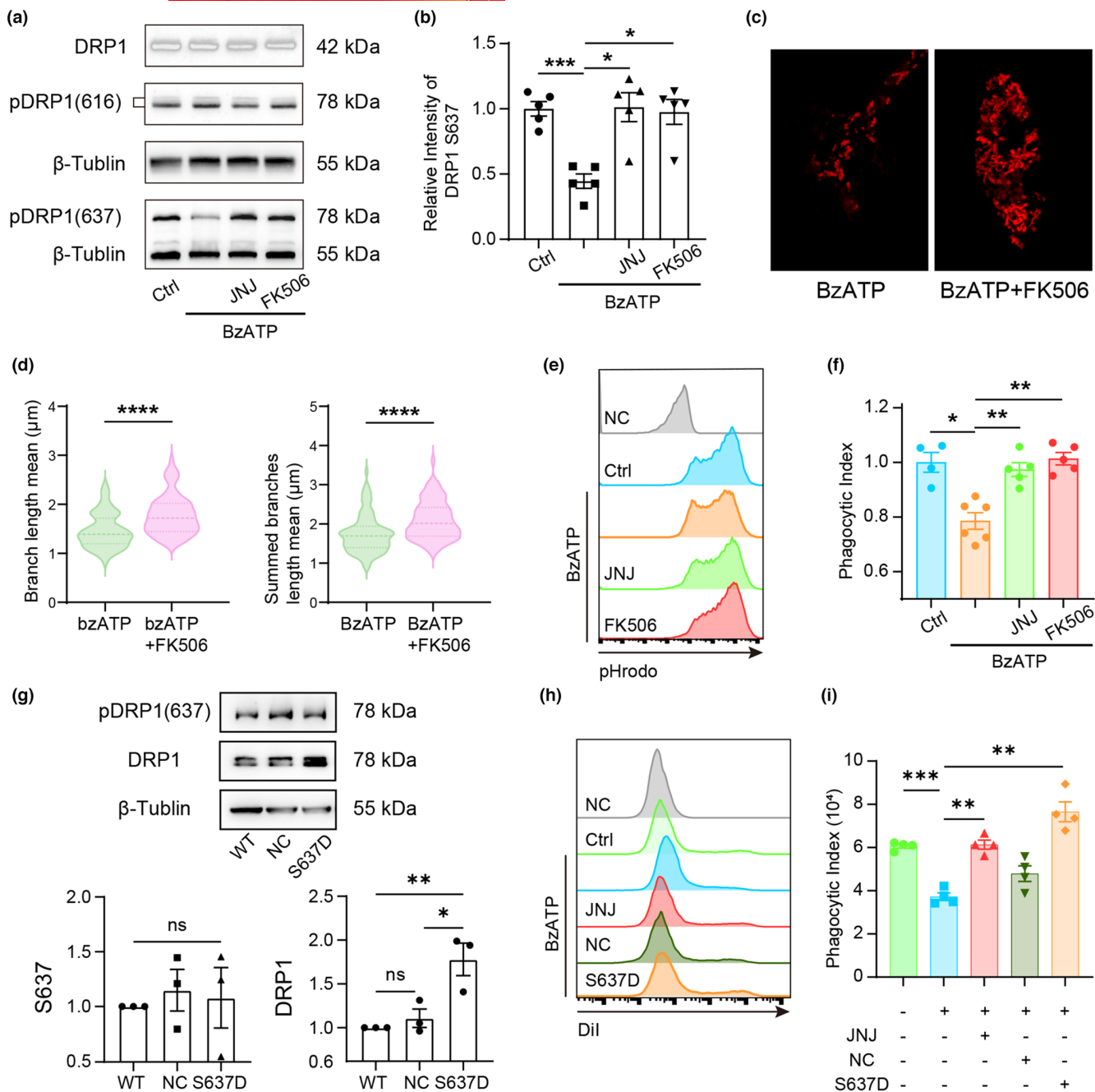
FIGURE 6 P2X7 activation promotes DRP1 S637 dephosphorylation by CaN. Microglia was treated with BzATP for 24 h in the presence of FK506 or not, then labelled with MitoTracker red. (a) Western blotting was used to assess DRP1 total protein, S616 phosphorylation and S637 phosphorylation. (b) Relative intensity analysis of S637 phosphorylation of DRP1. *N* denotes the number of independent cell culture preparations, *n* = 5 per group, Brown–Forsythe ANOVA with Dunnett's T3 test. (c) Representative pictures of mitochondria from two groups. (d) Branch length mean and summed branches length mean were counted with MiNA plugin. *N* denotes the number of pictures, *n* = 98 and 79, respectively, two-sided Mann–Whitney *U* test. (e, f) Microglia was stimulated with BzATP for 24 h after CaN was inhibited by FK506. Microglial phagocytosis was assessed by flow cytometry after CaN was inhibited. (g) Western blotting for S637D mutation efficiency. (h, i) Microglial phagocytosis was assessed by flow cytometry after S637D mutation. *N* denotes the number of independent cell culture preparations, *n* = 3–5 per group, one-way ANOVA with Tukey's test. NC, negative control; JNJ-47965567, JNJ for short in the panel; Exact *p* values noted; ns, not significant; *p < 0.05; **p < 0.01; ***p < 0.001, ****p < 0.05.

proliferation and activation after SAH (Figure 7c,d, 49.27% ± 3.30% vs. 25.10% ± 2.54%, *p* < 0.001). Then we labelled microglia and in-jured cells (mostly neuron according to our previous research (Tao et al., 2019)) with both Iba-1 and TUNEL, we observed that JNJ

significantly enhanced microglial phagocytosis of TUNEL+ neurons (Figure 7e,f, 25.00% (11.17%, 30.18%) vs. 28.57% (14.29%, 46.15%), *p* = 0.044). In addition, we stereotaxically injected DiO-labelled cell debris into the brain to assess microglial phagocytosis of cell debris
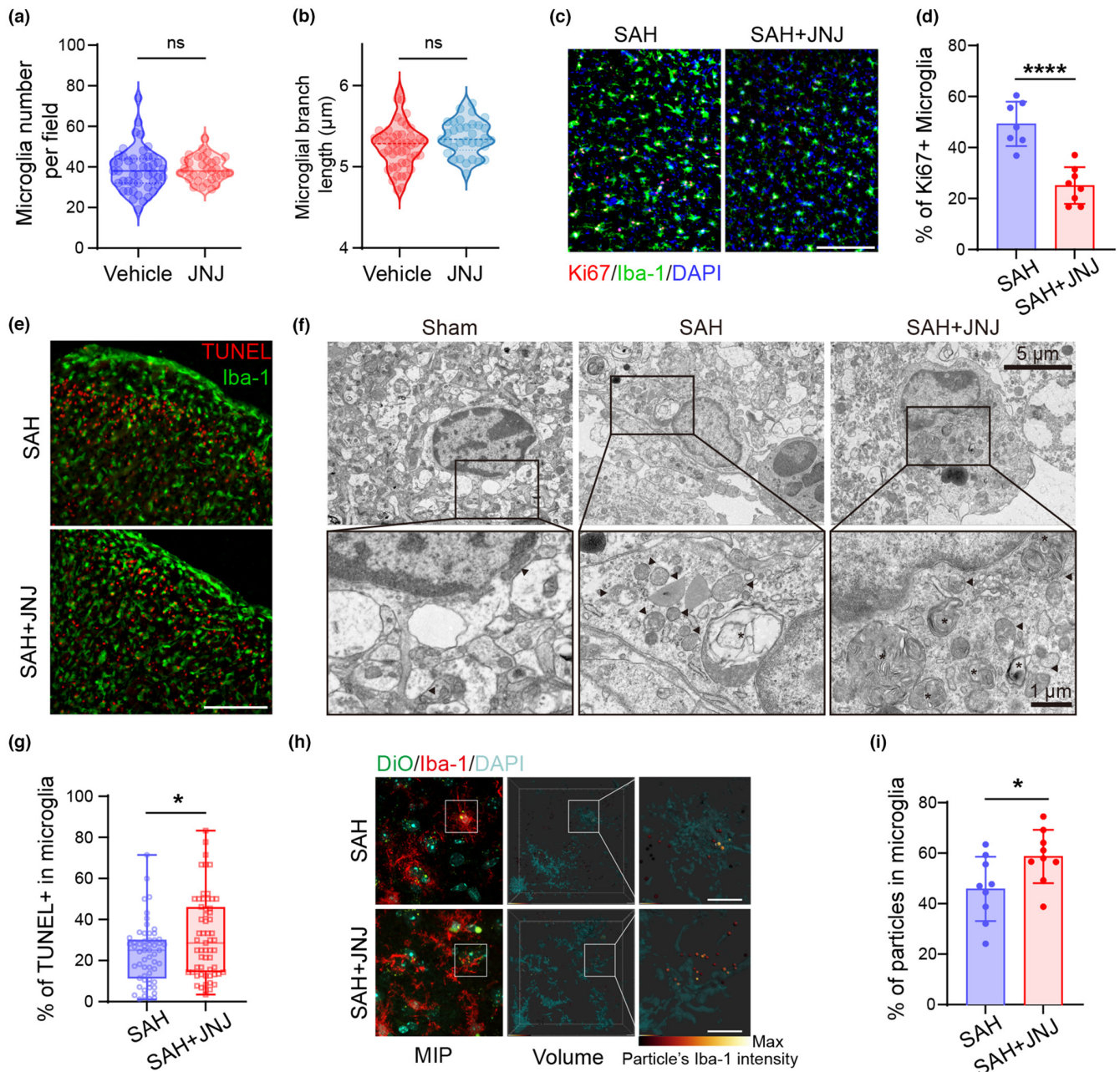
FIGURE 7 In mice, the inhibition of P2X7 limited the microglial proliferation but enhanced microglial phagocytosis. (a, b) The microglial population and morphology was assessed by IF after JNJ-47965567 was continuously (3d, bid) administered in the sham mice. *N* denotes the number of pictures, *n* = 47 pictures from 3 mice, and 33 pictures from 5 mice, respectively. Two-sided *t* test with Welch's correction. The SAH mice were continuously administered with JNJ-47965567 for 3 days (dpi 1–3). (c, d) Microglial proliferation was assessed by Ki67 (red) staining and the percentage of Ki67+ microglia (green) was analysed. *N* denotes the number of pictures, *n* = 7 pictures from 4 mice and 8 pictures from 4 mice, respectively. Two-sided Student's *t* test. Phagocytosis of TUNEL+ cells by microglia was assessed by IF. (e, g) Representative pictures the ratio of TUNEL+ cell in microglia: total TUNEL+ cell. *N* denotes the number of pictures, *n* = 57 pictures from 6 mice and 59 pictures from 7 mice, respectively. Two-sided Mann–Whitney *U* test, scale bar = 200 μm in panel (a, c & e). (f) Representative electron micrographs of microglia after SAH model. The black triangle refers to the mitochondria and the * refers to the phagocytic vesicles. Scale bar is shown in panel. Microglial phagocytosis was assessed after the stereotaxic injection of DiO-labelled cell debris (green). The particles in the 3D reconstructed images represent the DiO labelled cell debris, and their calibration colour indicates Iba-1 fluorescence intensity. Particles (green) were set with an appropriate threshold based on Iba-1 (red) fluorescence intensity, and particles within microglia were screened based on the threshold. (h) Representative images of microglial reconstruction and magnifications. (i) the % of particles inside microglia were analysed. *N* denotes the number of scans, *n* = 9 scans from 4 mice and 8 scans from 4 mice, respectively. Two-sided student's *t* test, scale bar = 10 μm. MIP, maximum intensity projection. JNJ-47965567, JNJ for short in the panel; Exact *p* values noted; ns, not significant; *$p < 0.05$; ****$p < 0.05$.

after SAH in vivo. 3D reconstruction and analysis revealed that JNJ increased the phagocytosis of membrane debris by microglia (Figure 7g,h, 45.82%±4.25% vs. 58.67%±3.52%, $p = 0.033$).

These observations all illustrate that inhibiting P2X7 activation in microglia after SAH can increase the phagocytic function of microglia, although it decreases the number of microglia in the injured area.

4 | DISCUSSION

P2X7 activation is a ubiquitous and important phenomenon that occurs after lesions. Damaged cells release high concentrations of ATP as chemokines to recruit microglia to the injury site and initiate a subsequent immune response, in which P2X7 is one of the most important receptors (Di Virgilio et al., 2017). An SAH study confirmed that blocking P2X7 causes a neuroprotective effect in SAH rats, but the mechanism is not known in detail (Chen et al., 2013). At present, it is believed that P2X7 is involved in the activation of NLRP3 and the release of IL-1β in microglia (Hu et al., 2015), which promotes the inflammatory response; on the other hand, P2X7 activation also leads to a decrease in microglial phagocytic function. Gu et al. concluded that P2X7 can act as a scavenger receptor without ATP stimulation, resulting in a decrease in cellular phagocytic function (Gu & Wiley, 2018).

In this study, we also confirmed that microglial phagocytosis is impaired under BzATP stimulation and described the curve of decreased phagocytosis under continuous P2X7 activation; we also noticed that specifically inhibiting P2X7 and blocking the influx of P2X7-triggered Ca^{2+} could alleviate the decrease in phagocytic function; we further clarified that Ca^{2+}/calcineurin/DRP1-mediated mitochondrial hyperfission is an important cause of phagocytic dysfunction, which provides a new understanding of the involvement of P2X7 in regulating the microglial phagocytic function.

Mitochondrial fission and fusion have an important impact on cellular functions, and the homeostasis of mitochondrial dynamics is vital to cellular functions (Bernier et al., 2020; Youle & van der Bliek, 2012). Mitochondrial fission produces mitochondria that contain less content and are more dispersed. Although reactive oxygen species are an essential process for cell proliferation, they are more likely to be produced after fission, and the ability to maintain mitochondrial membrane potential and produce ATP also decreases (Trevisan et al., 2018). Mitochondrial fusion, on the other hand, produces interconnected mitochondria, increases communication with the endoplasmic reticulum, and helps maintain the ability and homeostasis of mitochondria to produce ATP (Giacomello et al., 2020).

Mitochondrial dynamics also have an important impact on the function of immune cells (Joshi et al., 2019; Wang et al., 2017). Microglia/macrophages undergo excessive mitochondrial fission in response to stimulation by proinflammatory substances, such as LPS, and are accompanied by a transition in the main mode of energy supply to glycolysis (Nair et al., 2019). In several studies, mitochondrial fission was inhibited in microglia after LPS stimulation, and it was found that this inhibition can reduce the tendency of macrophages to convert to glycolysis and can reverse the proinflammatory microglial phenotypes (Katoh et al., 2017; Nair et al., 2019); therefore, targeting mitochondrial dynamics is a method to regulate the microglial phenotype. Our study confirmed that P2X7 inhibition was able to reverse mitochondrial fission after microglial activation and was able to significantly improve microglial phagocytosis. Although we did not explore changes in metabolic patterns in response to P2X7 activation or inhibition in detail, our conclusions validate the important influence of mitochondrial dynamics on the microglial activation phenotype.

Surprisingly, through our study in mice, we found that P2X7 inhibition impaired microglial proliferation under pathological conditions. The previous observation of P2X7 suggested that it was a death receptor and that its activation caused damage and even death to the cell (Gulbransen et al., 2012). However, an observation in microglia in vitro found that inhibition of P2X7 significantly reduced microglial activation and proliferation, and it was gradually recognized that P2X7 may have a role as a nutrient in immune cells (Monif et al., 2009). Further in vivo evidence was provided in our study, and at least in microglia, P2X7 is involved in the microglial activation and migration. Taken together with our observation, we suggest that P2X7 expression is increased in the early stage of injury, which facilitates microglial chemotaxis and proliferation to the lesion site but compromises microglial phagocytosis in the acute stage.

Our study provides new insights into the regulation of microglial activation and phagocytosis after SAH; however, this study also has some limitations. First, there are limitations in the quantification of microglial phagocytosis. Flow cytometry is the main foundation of microglial phagocytosis quantification in vitro, and phagocytosis is a dynamic and complex process. The phagocytic function of adherent cells must be different from that of microglia in brain tissue, which leads to some limitations in our results. Second, mitochondrial hyperfission under ATP stimulation must be further validated in vivo. To observe the morphology of mitochondria, high resolution and imaging quality is often necessary, and it is still difficult to observe mitochondrial dynamics in cells in vivo. Finally, continuous intraperitoneal injection of JNJ results in a reduced microglial population, which still to be further validated experimentally. Until the underlying mechanism is clear, the application of P2X7 inhibition treatment in vivo may be limited.

5 | CONCLUSION

In the present study, we found that the expression of microglial P2X7 increased after SAH and that the continued activation of P2X7 resulted in a gradual decrease in phagocytosis, while specifically blocking P2X7 activation reversed the impairment in phagocytosis. We then clarified that the impairment in phagocytosis was as a result of excessive mitochondrial fission, which was mediated by Ca^{2+}/calcineurin/DRP1, and that preventing excessive mitochondrial fission

could also alleviate phagocytic dysfunction. Our study deepens the understanding of microglial function after SAH and provides evidence for further regulation.

ORCID

Chun-hua Hang 🆔 https://orcid.org/0000-0001-8687-7599
Wei Li 🆔 https://orcid.org/0000-0002-9258-3500

REFERENCES

Ballabh, P., & de Vries, L. S. (2021). White matter injury in infants with intraventricular haemorrhage: Mechanisms and therapies. *Nature Reviews Neurology*, 17, 199–214. https://doi.org/10.1038/s41582-020-00447-8

Bernier, L.-P., York, E. M., & MacVicar, B. A. (2020). Immunometabolism in the brain: How metabolism shapes microglial function. *Trends in Neurosciences*, 43, 854–869. https://doi.org/10.1016/j.tins.2020.08.008

Bhattacharya, A., Wang, Q., Ao, H., Shoblock, J. R., Lord, B., Aluisio, L., Fraser, I., Nepomuceno, D., Neff, R. A., Welty, N., Lovenberg, T. W., Bonaventure, P., Wickenden, A. D., & Letavic, M. A. (2013). Pharmacological characterization of a novel centrally permeable P2X7 receptor antagonist: JNJ-47965567. *British Journal of Pharmacology*, 170, 624–640. https://doi.org/10.1111/bph.12314

Borges da Silva, H., Peng, C., Wang, H., Wanhainen, K. M., Ma, C., Lopez, S., Khoruts, A., Zhang, N., & Jameson, S. C. (2020). Sensing of ATP via the purinergic receptor P2RX7 promotes CD8+ Trm cell generation by enhancing their sensitivity to the cytokine TGF-β. *Immunity*, 53, 158–171.e6. https://doi.org/10.1016/j.immuni.2020.06.010

Cereghetti, G. M., Stangherlin, A., Martins de Brito, O., Chang, C. R., Blackstone, C., Bernardi, P., & Scorrano, L. (2008). Dephosphorylation by calcineurin regulates translocation of Drp1 to mitochondria. *Proceedings of the National Academy of Sciences of the United States of America*, 105, 15803–15808. https://doi.org/10.1073/pnas.0808249105

Chen, S., Ma, Q., Krafft, P. R., Chen, Y., Tang, J., Zhang, J., & Zhang, J. H. (2013). P2X7 receptor antagonism inhibits p38 mitogen-activated protein kinase activation and ameliorates neuronal apoptosis after subarachnoid hemorrhage in rats. *Crit Care Medicine*, 41, e466–e474. https://doi.org/10.1097/CCM.0b013e31829a8246

Chen, W., Zhang, Y., Zhai, X., Xie, L., Guo, Y., Chen, C., Li, Y., Wang, F., Zhu, Z., Zheng, L., Wan, J., & Li, P. (2022). Microglial phagocytosis and regulatory mechanisms after stroke. *Journal of Cerebral Blood Flow and Metabolism*, 42, 1579–1596. https://doi.org/10.1177/0271678X221098841

Coddou, C., Yan, Z., Obsil, T., Pablo Huidobro-Toro, J., & Stojilkovic, S. S. (2011). Activation and regulation of purinergic P2X receptor channels. *Pharmacological Reviews*, 63, 641–683. https://doi.org/10.1124/pr.110.003129

Colonna, M., & Butovsky, O. (2017). Microglia function in the central nervous system during health and neurodegeneration. *Annual Review of Immunology*, 35, 441–468. https://doi.org/10.1146/annurev-immunol-051116-052358

Crowley, L. C., Christensen, M. E., & Waterhouse, N. J. (2016). Measuring mitochondrial transmembrane potential by TMRE staining. *Cold Spring Harbor Protocols*, 12, 2016. https://doi.org/10.1101/pdb.prot087361

Davalos, D., Grutzendler, J., Yang, G., Kim, J. V., Zuo, Y., Jung, S., Littman, D. R., Dustin, M. L., & Gan, W.-B. (2005). ATP mediates rapid microglial response to local brain injury in vivo. *Nature Neuroscience*, 8, 752–758. https://doi.org/10.1038/nn1472

d'Errico, P., Ziegler-Waldkirch, S., Aires, V., Hoffmann, P., Mezö, C., Erny, D., Monasor, L. S., Liebscher, S., Ravi, V. M., Joseph, K., Schnell, O., Kierdorf, K., Staszewski, O., Tahirovic, S., Prinz, M., & Meyer-Luehmann, M. (2021). Microglia contribute to the propagation of Aβ into unaffected brain tissue. *Nature Neuroscience*, 1–6, 20–25. https://doi.org/10.1038/s41593-021-00951-0

Di Virgilio, F., Dal Ben, D., Sarti, A. C., Giuliani, A. L., & Falzoni, S. (2017). The P2X7 receptor in infection and inflammation. *Immunity*, 47, 15–31. https://doi.org/10.1016/j.immuni.2017.06.020

Etminan, N., Chang, H.-S., Hackenberg, K., de Rooij, N. K., Vergouwen, M. D. I., Rinkel, G. J. E., & Algra, A. (2019). Worldwide incidence of aneurysmal subarachnoid hemorrhage according to region, time period, blood pressure, and smoking prevalence in the population: A systematic review and meta-analysis. *JAMA Neurology*, 76, 588–597. https://doi.org/10.1001/jamaneurol.2019.0006

Francistiová, L., Bianchi, C., Di Lauro, C., Sebastián-Serrano, Á., de Diego-García, L., Kobolák, J., Dinnyés, A., & Díaz-Hernández, M. (2020). The role of P2X7 receptor in Alzheimer's disease. *Frontiers in Molecular Neuroscience*, 13, 94. https://doi.org/10.3389/fnmol.2020.00094

Garland, P., Durnford, A. J., Okemefuna, A. I., Dunbar, J., Nicoll, J. A. R., Galea, J., Boche, D., Bulters, D. O., & Galea, I. (2016). Heme-hemopexin scavenging is active in the brain and associates with outcome after subarachnoid hemorrhage. *Stroke*, 47, 872–876. https://doi.org/10.1161/STROKEAHA.115.011956

Giacomello, M., Pyakurel, A., Glytsou, C., & Scorrano, L. (2020). The cell biology of mitochondrial membrane dynamics. *Nature Reviews.*

Molecular Cell Biology, 21, 204–224. https://doi.org/10.1038/s4158 0-020-0210-7

Gu, B. J., Saunders, B. M., Jursik, C., & Wiley, J. S. (2010). The P2X7-nonmuscle myosin membrane complex regulates phagocytosis of nonopsonized particles and bacteria by a pathway attenuated by extracellular ATP. *Blood*, 115, 1621–1631. https://doi.org/10.1182/blood-2009-11-251744

Gu, B. J., & Wiley, J. S. (2018). P2X7 as a scavenger receptor for innate phagocytosis in the brain: Phagocytic role of P2X7 receptor. *British Journal of Pharmacology*, 175, 4195–4208. https://doi.org/10.1111/bph.14470

Gulbransen, B. D., Bashashati, M., Hirota, S. A., Gui, X., Roberts, J. A., MacDonald, J. A., Muruve, D. A., McKay, D. M., Beck, P. L., Mawe, G. M., Thompson, R. J., & Sharkey, K. A. (2012). Activation of neuronal P2X7 receptor–pannexin-1 mediates death of enteric neurons during colitis. *Nature Medicine*, 18, 600–604. https://doi.org/10.1038/nm.2679

Hu, S. J., Calippe, B., Lavalette, S., Roubeix, C., Montassar, F., Housset, M., Levy, O., Delarasse, C., Paques, M., Sahel, J.-A., Sennlaub, F., & Guillonneau, X. (2015). Upregulation of P2RX7 in Cx3cr1-deficient mononuclear phagocytes leads to increased interleukin-1β secretion and photoreceptor neurodegeneration. *The Journal of Neuroscience*, 35, 6987–6996. https://doi.org/10.1523/JNEUROSCI.3955-14.2015

Jimenez-Pacheco, A., Diaz-Hernandez, M., Arribas-Blázquez, M., Sanz-Rodriguez, A., Olivos-Oré, L. A., Artalejo, A. R., Alves, M., Letavic, M., Miras-Portugal, M. T., Conroy, R. M., Delanty, N., Farrell, M. A., O'Brien, D. F., Bhattacharya, A., Engel, T., & Henshall, D. C. (2016). Transient P2X7 receptor antagonism produces lasting reductions in spontaneous seizures and gliosis in experimental temporal lobe epilepsy. *The Journal of Neuroscience*, 36, 5920–5932. https://doi.org/10.1523/JNEUROSCI.4009-15.2016

Joshi, A. U., Minhas, P. S., Liddelow, S. A., Haileselassie, B., Andreasson, K. I., Dorn, G. W., & Mochly-Rosen, D. (2019). Fragmented mitochondria released from microglia trigger A1 astrocytic response and propagate inflammatory neurodegeneration. *Nature Neuroscience*, 22, 1635–1648. https://doi.org/10.1038/s4159 3-019-0486-0

Katoh, M., Wu, B., Nguyen, H. B., Thai, T. Q., Yamasaki, R., Lu, H., Rietsch, A. M., Zorlu, M. M., Shinozaki, Y., Saitoh, Y., Saitoh, S., Sakoh, T., Ikenaka, K., Koizumi, S., Ransohoff, R. M., & Ohno, N. (2017). Polymorphic regulation of mitochondrial fission and fusion modifies phenotypes of microglia in neuroinflammation. *Scientific Reports*, 7, 4942. https://doi.org/10.1038/s41598-017-05232-0

Lan, X., Han, X., Li, Q., Yang, Q.-W., & Wang, J. (2017). Modulators of microglial activation and polarization after intracerebral haemorrhage. *Nature Reviews. Neurology*, 13, 420–433.

Lloyd, A. F., Davies, C. L., Holloway, R. K., Labrak, Y., Ireland, G., Carradori, D., Dillenburg, A., Borger, E., Soong, D., & Richardson, J. C. (2019). Central nervous system regeneration is driven by microglia necroptosis and repopulation. *Nature Neuroscience*, 22, 1046–1052. https://doi.org/10.1038/s41593-019-0418-z

Macdonald, R. L., & Schweizer, T. A. (2016). Spontaneous subarachnoid haemorrhage. *Lancet*, 389, 655–666. https://doi.org/10.1016/S0140-6736(16)30668-7

Martínez-García, J. J., Martínez-Banaclocha, H., Angosto-Bazarra, D., de Torre-Minguela, C., Baroja-Mazo, A., Alarcón-Vila, C., Martínez-Alarcón, L., Amores-Iniesta, J., Martín-Sánchez, F., Ercole, G. A., Martínez, C. M., González-Lisorge, A., Fernández-Pacheco, J., Martínez-Gil, P., Adriouch, S., Koch-Nolte, F., Luján, J., Acosta-Villegas, F., Parrilla, P., … Pelegrin, P. (2019). P2X7 receptor induces mitochondrial failure in monocytes and compromises NLRP3 inflammasome activation during sepsis. *Nature Communications*, 10, 2711. https://doi.org/10.1038/s41467-019-10626-x

McCarthy, A. E., Yoshioka, C., & Mansoor, S. E. (2019). Full-length P2X7 structures reveal how palmitoylation prevents channel desensitization. *Cell*, 179, 659–670.e13. https://doi.org/10.1016/j.cell.2019.09.017

McSweeney, C., & Mao, Y. (2015). Applying stereotactic injection technique to study genetic effects on animal behaviors. *Journal of Visualized Experiments*, 52653, e52653. https://doi.org/10.3791/52653

Monif, M., Reid, C. A., Powell, K. L., Smart, M. L., & Williams, D. A. (2009). The P2X7 receptor drives microglial activation and proliferation: A trophic role for P2X7R pore. *The Journal of Neuroscience*, 29, 3781–3791. https://doi.org/10.1523/JNEUROSCI.5512-08.2009

Nair, S., Sobotka, K. S., Joshi, P., Gressens, P., Fleiss, B., Thornton, C., Mallard, C., & Hagberg, H. (2019). Lipopolysaccharide-induced alteration of mitochondrial morphology induces a metabolic shift in microglia modulating the inflammatory response in vitro and in vivo. *Glia*, 67, 1047–1061. https://doi.org/10.1002/glia.23587

Pang, J., Peng, J., Yang, P., Kuai, L., Chen, L., Zhang, J. H., & Jiang, Y. (2019). White matter injury in early brain injury after subarachnoid hemorrhage. *Cell Transplantation*, 28, 26–35. https://doi.org/10.1177/0963689718812054

Park, Y., Abihssira-García, I. S., Thalmann, S., Wiegertjes, G. F., Barreda, D. R., Olsvik, P. A., & Kiron, V. (2020). Imaging flow cytometry protocols for examining phagocytosis of microplastics and bioparticles by immune cells of aquatic animals. *Frontiers in Immunology*, 11, 203. https://doi.org/10.3389/fimmu.2020.00203

Podleśny-Drabiniok, A., Marcora, E., & Goate, A. M. (2020). Microglial phagocytosis: A disease-associated process emerging from Alzheimer's disease genetics. *Trends in Neurosciences*, 43, 965–979. https://doi.org/10.1016/j.tins.2020.10.002

Priller, J., & Prinz, M. (2019). Targeting microglia in brain disorders. *Science*, 365, 32–33.

Rodrigues, R. J., Tomé, A. R., & Cunha, R. A. (2015). ATP as a multi-target danger signal in the brain. *Frontiers in Neuroscience*, 9, 148. https://doi.org/10.3389/fnins.2015.00148

Romagnani, A., Rottoli, E., Mazza, E. M. C., Rezzonico-Jost, T., Conti, B. D. P., Proietti, M., Perotti, M., Civanelli, E., Perruzza, L., Catapano, A. L., Baragetti, A., Tenedini, E., Tagliafico, E., Falzoni, S., Virgilio, F. D., Norata, G. D., Bicciato, S., & Grassi, F. (2020). P2X7 receptor activity limits accumulation of T cells within tumors. *Cancer Research*, 80, 3906–3919. https://doi.org/10.1158/0008-5472.CAN-19-3807

Rudolph, M., Schmeer, C. W., Günther, M., Woitke, F., Kathner-Schaffert, C., Karapetow, L., Lindner, J., Lehmann, T., Jirikowski, G., Witte, O. W., Redecker, C., & Keiner, S. (2021). Microglia-mediated phagocytosis of apoptotic nuclei is impaired in the adult murine hippocampus after stroke. *Glia*, 69, 2006–2022. https://doi.org/10.1002/glia.24009

Savage, J. C., Picard, K., González-Ibáñez, F., & Tremblay, M.-.È. (2018). A brief history of microglial ultrastructure: Distinctive features, phenotypes, and functions discovered over the past 60 years by electron microscopy. *Frontiers in Immunology*, 9, 803. https://10.3389/fimmu.2018.00803

Schallner, N., Pandit, R., LeBlanc, R., Thomas, A. J., Ogilvy, C. S., Zuckerbraun, B. S., Gallo, D., Otterbein, L. E., & Hanafy, K. A. (2015). Microglia regulate blood clearance in subarachnoid hemorrhage by heme oxygenase-1. *The Journal of Clinical Investigation*, 125, 2609–2625. https://doi.org/10.1172/JCI78443

Schüller, K., Bühler, D., & Plesnila, N. (2013). A murine model of subarachnoid hemorrhage. *Journal of Visualized Experiments*, 81, e50845. https://doi.org/10.3791/50845

Sen, M. K., Mahns, D. A., Coorssen, J. R., & Shortland, P. J. (2022). The roles of microglia and astrocytes in phagocytosis and myelination: Insights from the cuprizone model of multiple sclerosis. *Glia n/*, 70, 1215–1250. https://doi.org/10.1002/glia.24148

Shieh, C.-H., Heinrich, A., Serchov, T., van Calker, D., & Biber, K. (2014). P2X7-dependent, but differentially regulated release of IL-6, CCL2,

and TNF-α in cultured mouse microglia. *Glia*, *62*, 592–607. https://doi.org/10.1002/glia.22628

Tao, T., Liu, G.-J., Shi, X., Zhou, Y., Lu, Y., Gao, Y.-Y., Zhang, X.-S., Wang, H., Wu, L.-Y., Chen, C.-L., Zhuang, Z., Li, W., & Hang, C.-H. (2019). DHEA attenuates microglial activation via induction of JMJD3 in experimental subarachnoid Haemorrhage. *Journal of Neuroinflammation*, *16*, 243. https://doi.org/10.1186/s12974-019-1641-y

Trevisan, T., Pendin, D., Montagna, A., Bova, S., Ghelli, A. M., & Daga, A. (2018). Manipulation of mitochondria dynamics reveals separate roles for form and function in mitochondria distribution. *Cell Reports*, *23*, 1742–1753. https://doi.org/10.1016/j.celrep.2018.04.017

Valente, A. J., Maddalena, L. A., Robb, E. L., Moradi, F., & Stuart, J. A. (2017). A simple ImageJ macro tool for analyzing mitochondrial network morphology in mammalian cell culture. *Acta Histochemica*, *119*, 315–326. https://doi.org/10.1016/j.acthis.2017.03.001

Van Broeckhoven, J., Sommer, D., Dooley, D., Hendrix, S., & Franssen, A. J. P. M. (2021). Macrophage phagocytosis after spinal cord injury: When friends become foes. *Brain*, *144*, 2933–2945. https://doi.org/10.1093/brain/awab250

Wang, Y., Subramanian, M., Yurdagul, A., Barbosa-Lorenzi, V. C., Cai, B., de Juan-Sanz, J., Ryan, T. A., Nomura, M., Maxfield, F. R., & Tabas, I. (2017). Mitochondrial fission promotes the continued clearance of apoptotic cells by macrophages. *Cell*, *171*, 331–345.e22. https://doi.org/10.1016/j.cell.2017.08.041

Wolf, S. A., Boddeke, H. W. G. M., & Kettenmann, H. (2017). Microglia in physiology and disease. *Annual Review of Physiology*, *79*, 619–643. https://doi.org/10.1146/annurev-physiol-022516-034406

Youle, R. J., & van der Bliek, A. M. (2012). Mitochondrial fission, fusion, and stress. *Science*, *337*, 1062–1065. https://doi.org/10.1126/science.1219855

SUPPORTING INFORMATION

Additional supporting information can be found online in the Supporting Information section at the end of this article.

How to cite this article: Tao, T., Chen, X., Zhou, Y., Zheng, Q., Gao, S., Wang, J., Ding, P., Li, X., Peng, Z., Lu, Y., Gao, Y., Zhuang, Z., Hang, C.-h., & Li, W. (2022). Continued P2X7 activation leads to mitochondrial fission and compromising microglial phagocytosis after subarachnoid haemorrhage. *Journal of Neurochemistry*, *163*, 419–437. https://doi.org/10.1111/jnc.15712